Research Article

Aditya Rio Prabowo*, Ridwan Ridwan, Tuswan Tuswan, Jung Min Sohn, Eko Surojo, and Fitrian Imaduddin

Effect of the selected parameters in idealizing material failures under tensile loads: Benchmarks for damage analysis on thin-walled structures

https://doi.org/10.1515/cls-2022-0021
Received Nov 28, 2021; accepted Feb 10, 2022

Abstract: The development of the global economy has led to a rise in ship traffic. As a result, the risk of accidents, such as collisions between ships and grounding, has also increased. Different failure criteria to capture these accidents have been introduced by researchers. Therefore, the purpose of this study was to determine the essential distinction between these failure criteria. The simulations suggest that failure criteria based on the maximum stress result in a slightly higher rupture strain value, greater crack propagation, and higher internal energy than those based on the maximum strain. Furthermore, using a larger mesh size compared with the size of the test specimen appears to greatly affect the validity of the simulation results.

Keywords: finite element method; tensile test; rupture strain; failure phenomena; ship collision modeling

***Corresponding Author: Aditya Rio Prabowo:** Department of Mechanical Engineering, Universitas Sebelas Maret, Surakarta 57126, Indonesia; Email: aditya@ft.uns.ac.id
Ridwan Ridwan: Department of Mechanical Engineering, Universitas Merdeka Madiun 63133, Madiun, Indonesia
Tuswan Tuswan: Department of Naval Architecture, Universitas Diponegoro, Semarang 50275, Indonesia
Jung Min Sohn: Department of Naval Architecture and Marine Systems Engineering, Pukyong National University, Busan 48513, South Korea
Eko Surojo: Department of Mechanical Engineering, Universitas Sebelas Maret, Surakarta 57126, Indonesia
Fitrian Imaduddin: Department of Mechanical Engineering, Universitas Sebelas Maret, Surakarta 57126, Indonesia; Department of Mechanical Engineering, Islamic University of Madinah, Medina 42351, Saudi Arabia

1 Introduction

The maritime transportation system is an important component of the global economy and significantly contributes to the fulfillment of numerous demands. In 2018, approximately 11 billion tons of cargo were transported by sea [1]. As transportation vessels, ships have an important role in these activities. Moreover, maritime transportation, especially via ship, has become common, and the number of vessels continues to increase due to their efficiency. These vessels are a vital part of existing communication systems. However, as the number of ships increases, the probability of accidents rises. Ship–ship collision and grounding events are now among the most catastrophic accidents and can cause the loss of lives, damage to the environment, economic losses, and other detrimental effects [2–5]. Numerous international projects and studies have been presented with the aim of enhancing many different aspects of maritime safety, such as ship operation, advanced ship designs, intact and damage stability, evacuation, and rescue.

In the classical ship collision theory, the collision estimation is typically separated into two independent problems: external and internal collision dynamics. External collision dynamics pertain to the motion of colliding ships and their interaction with the surrounding water. On the other hand, the internal dynamics involve the local crushing of material in the ship structures involved in the collision [6].

Methods for the analysis of structural damage in ship collisions and grounding can be classified into four categories: empirical methods [7], finite element methods [8–14], experimental methods, and simplified analytical methods. In a situation where an accident occurs very quickly, i.e., collisions between ships, the impact can inflict extremely severe damage to the material and structure. As the impact occurs in a short period, the material used in the ship structure can fail without significant elongation. In the past three decades, several failure criteria to capture this failure condition have been introduced by different researchers.

The most common failure criterion used for ship collision numerical modeling is the equivalent plastic strain criterion [15]. In the early 2000s, failure criteria based on maximum strain were developed by Germanischer Lloyd [16] and Peschmann [17]. Some failure criteria benchmark studies using Germanischer Lloyd and Peschmann simulating the collision response of ship side structures were investigated by Ehlers *et al.* [18], and crashworthiness assessment of powered-hard grounding accidents was simulated by Prabowo *et al.* [19]. In addition, failure criteria based on maximum stress have also been developed, such as the Rice-Tracey, and Cockcroft-Latham (RTCL) criterion proposed by Törnqvist [20], which is based on the combination of two continuum damage models: the Rice-Tracey [21] and Cockcroft-Latham [22] damage models. Moreover, failure criteria based on ultimate strain are reviewed in the works of literature [23–26]. Most of the reported studies have used failure criteria on immensely complex external collision dynamics in different conditions, such as collision, grounding, etc. [8–14, 27–29].

Although many previous investigations have explored failure criteria used in ship collision numerical modeling, few studies have evaluated the numerical response differences between stress-based failure criteria and strain-based failure criteria in numerical modeling with various numerical parameters, including specimen topology, mesh size, and applied material types. In this study, three failure criteria- Germanischer Lloyd (GL), Peschmann, Rice-Tracey, and Cockcroft-Latham (RTCL) criteria-were applied in numerical modeling using ANSYS software. The main purpose of this study was to determine the highest failure strain among the three failure criteria. The tensile test was used as a failure model, and the use of the specimen was also investigated to obtain satisfactory results.

2 Literature review

In this section, a theoretical framework is introduced to support a substantive theory of recent work. The contents cover the formulation of finite element method, nonlinear dynamic algorithm, fundamental of tensile test, and Tresca and von Mises yield criteria.

2.1 Governing equation in finite element formulation

The following procedure is applied in the finite element method [30]. The procedure concerns the global discrete equilibrium equation, where the conservation of mass can be written in matrix form for a given time t. For the quasi-static case, the input in matrix form is the working load or force. The relationship between the residual vector R_U and the force can be written as:

$$R_U = F_U - F_\sigma = 0 \tag{1}$$

where F_U and F_σ are the external and internal force vectors, respectively. R_U is calculated for the initial configuration by employing the total Lagrangian method [31, 32].

In the case of the element expressions, the discretized equilibrium equation of these vectors can be written as in Eq. (2) and Eq. (3).

$$F_U^{(e)} = \int_{\Omega_0^{(e)}} N_U^T b_{F_0} d\Omega_0 + \int_{\Gamma_{\sigma_0}^{(e)}} N_U^T \bar{t}_0 d\Gamma_{\sigma_0} + \sum_{j=1}^{n_{cU}} F_{c_{Uj}}^{(e)} \tag{2}$$

$$F_\sigma^{(e)} = \int_{\Omega_0^{(e)}} B^T S d\Omega_0 \tag{3}$$

where N_U and b_{F_0} are the shape function matrix for displacements and the body force vector at the initial configuration Ω_0, respectively. $\bar{t}_0$ is the traction vector at boundary $\Gamma_{\sigma_0} \subset \Gamma_0$ ($\Gamma_0 = \partial\Omega_0$), $F_{c_U}^{(e)}$ is the point force vector at element *(e)*, and n_{c_U} is a loaded node. $\bar{B}$ is the strain-displacement matrix for large strains [33]. $S = JF^{-1} \cdot \sigma \cdot F^{-T}$ is the Second Piola-Kirchhoff stress tensor, and the superscript T is the transpose symbol.

In an iterative process (Newton-Raphson), the following Jacobian matrix is required:

$$J_{UU} = -\frac{\partial R_U}{\partial U} \cong K_U \tag{4}$$

$$K_U^{(e)} = \int_{\Omega_0^{(e)}} \bar{B}^T \frac{\partial S}{\partial E} \bar{B} d\Omega_0 + \int_{\Omega_0^{(e)}} \bar{H}^T S H d\Omega_0 \tag{5}$$

where K_U is the stiffness matrix. U and $\partial S/\partial E$ are the nodal displacement vector and the tangent elastoplastic constitutive tensor for the initial configuration Ω_0, E is the Green–Lagrange strain tensor, and $\bar{H}$ is the strain-displacement matrix for large strains derived by the linearization of $\bar{B}$.

2.2 Brief characteristics of the dynamic algorithm, software, and computer

The nonlinear dynamic analyses in this study were performed using the ANSYS Explicit Dynamics code [34]. The algorithm implemented in this code is characterized as:

$$\{a_t\} = [M]^{-1} \left(\left\{ F_t^{ext} \right\} - \left\{ F_t^{int} \right\} \right) \tag{6}$$

$$F^{int} = \sum \left(\int_{\Omega} \left(B^T \sigma_n d\Omega + F^{hg} \right) + F^{cont} \right) \tag{7}$$

where $\{a_t\}$ is the acceleration at time t, and $[M]$ is the mass matrix. $\left\{F_t^{ext}\right\}$ is the applied external and body force vector, and $\left\{F_t^{int}\right\}$ is the internal force vector. F^{hg} is the hourglass resistance force, and B^T is the form identical to the linear discrete strain-displacement matrix. F^{cont} is the contact force, Ω is the solid volume, and σ_n is the internal stress. In this algorithm, the velocities and displacements are evaluated as follows:

$$\left\{v_{t+\Delta t/2}\right\} = \left\{v_{t-\Delta t/2}\right\} + \{a_t\}\,\Delta t_t \tag{8}$$

$$\{u_{t+\Delta t}\} = \{u_t\} + \left\{v_{t+\Delta t/2}\right\}\Delta t_{t+\Delta t/2} \tag{9}$$

$$\{x_{t+\Delta t}\} = \{x_0\} + \{u_{t+\Delta t}\} \tag{10}$$

where $\{v_t\}$ is the velocity at time t, and $\{u_t\}$ is the displacement at time t. $\{x_0\}$is the initial geometry, and $\{x_t\}$ is the updated geometry at time t. Δt_t is the difference in time at time t compared with the initial/selected condition.

2.3 Tensile test: fundamentals

The material response to mechanical loads is often measured by performing a uniaxial tensile test. Typically, the elongation of the sample is measured by a change in gauge length (l), and the results are displayed as a load–extension curve or an engineering stress-strain curve. In ductile material, the first region of the stress-strain curve shows elasticity until reaching a certain load. After passing through the elastic region, the ductile material will deform plastically and fail. On the other hand, brittle material fails without plastic deformation [35–37].

A tensile test specimen is presented in Figure 1. The middle of the specimen is the original gauge length l_0 and is where the failure is expected to occur. During the test, the applied load F and the elongation $\Delta L = l - l_0$ are recorded. The load F is divided by the original cross-sectional area of specimen A_0, and the elongation ΔL is divided by the original gauge length l_0. The engineering stress $\sigma_{eng.}$ is defined as:

$$\sigma_{eng.} = \frac{F}{A_0} \tag{11}$$

and the engineering strain $e_{eng.}$ is:

$$e_{eng.} = \frac{\Delta L}{l_0} \tag{12}$$

There are several conditions on the stress-strain curve. One of the conditions that can be seen is the occurrence of the nonlinear curve phenomenon. This condition is caused by strain hardening, which results primarily from an increasing dislocation density that increases the strength of the material [37]. As a result, the material is permanently deformed, and the load–deformation relationship in this plastic region is nonlinear.

The engineering stress definitions are based on the original cross-sectional area A_0 rather than the current value A. Furthermore, the engineering strain is also based on the original gauge length l_0 instead of the instantaneous gauge length l. To solve these conditions, the true stress σ and true strain ε are introduced and defined as [36]:

$$\sigma = \frac{F}{A} \tag{13}$$

Hence, A is the instantaneous cross-sectional area of the test specimen. The plastic deformation takes place without any appreciable change in volume. The volume of the material before deformation is equal to the volume after deformation:

$$A_0 l_0 = Al \tag{14}$$

$$\sigma = \frac{F}{A_0}\frac{l}{l_0} = \sigma_{eng.}\,(1 + e_{eng.}) \tag{15}$$

$$\varepsilon = \int_{l_0}^{l} \frac{dl}{l} = \ln\left(\frac{l}{l_0}\right) = \ln\left(1 + \frac{\Delta l}{l_0}\right) = \ln\,(1 + e_{eng.}) \tag{16}$$

The true stress-strain curve does not reach a maximum as in an engineering curve, and the strain value is valid in the range from uniform elongation to the onset of necking.

For the plastic region of the true stress-true strain curve, the relationship between stress and strain is nonlinear. A common empirical stress-strain relationship is Hollomon's (power) law [38]:

$$\sigma = K\varepsilon^n \tag{17}$$

where K is the strength coefficient, and the exponent n is the strain-hardening exponent.

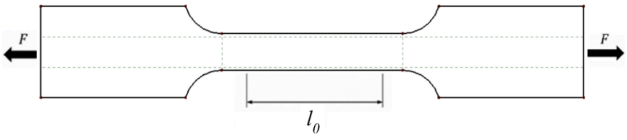

Figure 1: Typical tensile test specimen

2.4 Yield criteria

The yield criteria define the limit of elastic behavior or the start of plastic deformation in material under multi-axial states of stress. A criterion for determining the condition of continuous plastic flow is defined as the flow criterion [39]. In a uniaxial compression or tensile test, the material starts to flow plastically when the stress in the material reaches the material yield strength:

$$\sigma = \frac{F}{A} = \sigma_f \tag{18}$$

Hence, F is the instantaneous load, A is the instantaneous cross-sectional area of the specimen, and σ_f is the yield strength of the material and called the flow stress.

Several theories have been developed for predicting the stress under which a material element will deform plastically. The most popular yield criteria used in numerical modeling are the Tresca yield criterion and the von Mises yield criterion.

The Tresca yield criterion is based on the assumption that the material starts to yield when the greatest maximum shear stress reaches a critical value:

$$\max\left\{|\sigma_1 - \sigma_2|, |\sigma_2 - \sigma_3|, |\sigma_3 - \sigma_1|\right\} = \sigma_f \tag{19}$$

where σ_1, σ_2, and σ_3 are principal stresses, and σ_f is the flow stress. Hence, under the principal stress condition, Eq. (19) becomes:

$$|\sigma_1 - \sigma_2| = \sigma_f \tag{20}$$

The Tresca yield criterion in the principal stress space is depicted graphically by the hexagon in Figure 2.

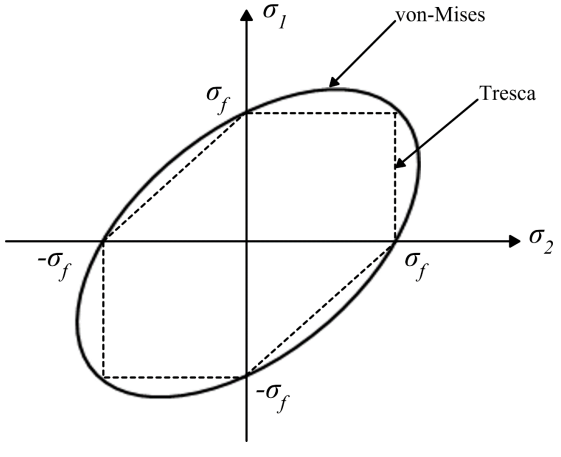

Figure 2: Comparison of the yield locus for the plane stress of von Mises yield criterion and Tresca yield criterion

In contrast to the Tresca yield criterion, the von Mises yield criterion considers all principal shear stresses. The von Mises criterion can be expressed in terms of principal stresses:

$$\sqrt{\frac{1}{2}\left\{(\sigma_1 - \sigma_2)^2 + (\sigma_2 - \sigma_3)^2 + (\sigma_3 - \sigma_1)^2\right\}} = \sigma_f \tag{21}$$

The von Mises yield criterion in the principal stress space is depicted graphically by the ellipse in Figure 2. The two yield criteria have major mathematical differences, although the values of predicted stress do not differ by more than 15% [40].

2.5 Failure phenomena

Marine structures must be designed to have a long and safe operational life and the lowest possible risk of catastrophic failures. However, with the constant demand for structures with decreased weight and the ability to withstand increased loads, failures can occur due to one or several of the following causes: collision and grounding [40, 41], yielding, fatigue, corrosion [42], creep, etc.

Recently, several failures of marine structures, such as ship structures, have occurred. For instance, in 2013, the container ship MOL Comfort (316 m length) suffered a structural failure, as shown in Figure 3a. The analysis results showed that the bottom shell plates experienced plastic deformation in the transverse direction just before the longitudinal hull girders of the ship experienced the maximum load [43]. Furthermore, the crack in the middle of the ship was exacerbated by bad weather at the time. Figure 3b shows a failure in the ship hull panel under indentation in the experimental laboratory [44]. The plates were made from mild steel (S235JR EN10025) with 5 mm thickness. In this case, the failure was largely the result of a significant stretch of the membrane. The strength of this structure was found to be able to bear a load of 1500 kN.

At a laboratory scale, failures in marine structures are generally analyzed using the finite element analysis (FEA) method as a solver. In 2020, the failure mechanism of a tanker's side structures under indenter pressure was investigated using the FEA method, as presented in Figure 4. The damage model and the occurrence of folding can be clearly observed. Figure 4b shows the FEA of the failure of rectangular steel plates struck laterally by hemispherical indenters, and the results are in good accordance with the experimental outcome. The use of FEA can reduce the cost of experiments while providing fairly accurate results. However, aspects such as failure criteria, boundary conditions, and mesh size selection are crucial considerations.

(a) (b)

Figure 3: (a) Collapsed structures of MOL Comfort container ship [43] and (b) indentation of ship hull panels after fracture [44]

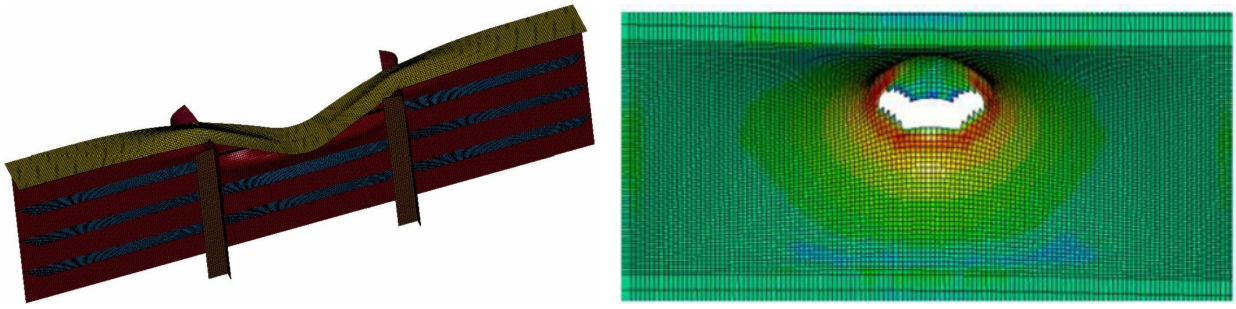

(a) (b)

Figure 4: (a) Failure mechanism of a tanker's side structures [45]; (b) failure of the plate after the impact [46]

2.6 Failure criteria

In this section, the constitutive model and research progress of different failure criteria are reviewed. There are four different failure criteria that will be investigated in this work, including Gremanischer Lloyd criterion, Peschmann criterion, Rice-Tracey and Cockcroft-Latham criterion, and ultimate strain criterion. As mentioned previously, the four failure criteria were implemented as user-defined material models in a software subroutine.

2.6.1 Germanischer Lloyd criterion

The Germanischer Lloyd (GL) criterion [16] is based on a through-thickness strain experiment on a damaged plate. This criterion was developed from the actual structure of a ship that experienced a collision and grounding accident. Eq. (22) is known as the Germanischer Lloyd (GL) criterion, which assumes that at the moment of fracture, the element can be expressed as:

$$\varepsilon_f (l_e) = \varepsilon_g + \varepsilon_e \left(\frac{t}{l_e} \right) \tag{22}$$

where ε_g is the uniform strain, ε_e is the necking strain, and t and l_e are the thickness and length of the element, respectively. For mild steel, which is commonly used in shipbuilding, the uniform and necking strains were measured and determined to have the following values [47]: $\varepsilon g = 0.056$ and $\varepsilon e = 0.54$. These values were obtained by BV based on measurements of damaged ships that experienced real accidents. Unfortunately, no literature could be found that mentions the specific type of mild steel that obtained these values. Previous studies that used the Germanischer Lloyd criterion are listed in Table 1.

Table 1: Research that used the Germanischer Lloyd criterion

No.	Research title	Methodology	Author	Year
1	Simulating the collision response of ship side structures: A failure criteria benchmark study	FE analysis	Ehlers *et al.* [18]	2008
2	Crashworthiness assessment of thin-walled bottom structures during powered-hard grounding accidents	FE analysis	Prabowo *et al.* [19]	2018
3	Benchmark study of failure criteria for ship collision modeling using purpose-designed tensile specimen geometries	Experiment and FE analysis	Calle *et al.* [2]	2017a

Table 2: Research that used the Peschmann criterion

No.	Research title	Methodology	Author	Year
1	Energy absorption by the steel structure of ships in the event of collisions	Experiment and FE analysis	Lehmann and Peschmann [8]	2002
2	Simulating the collision response of ship side structures: A failure criteria benchmark study	FE analysis	Ehlers *et al.* [18]	2008
3	Crashworthiness assessment of thin-walled bottom structures during powered-hard grounding accidents	FE analysis	Prabowo *et al.* [19]	2018
4	Benchmark study of failure criteria for ship collision modeling using purpose-designed tensile specimen geometries	Experiment and FE analysis	Calle *et al.* [2]	2017a

2.6.2 Peschmann criterion

The Peschmann criterion was proposed by Peschmann [17] and is commonly applied in numerical models of ship collisions to describe energy absorption due to plastic deformation. The formulation of the Peschmann criterion is based on a forming limit diagram that was obtained experimentally to evaluate the equivalent plastic strain at different locations at the moment of fracture with the given relation:

$$\varepsilon_f(l_e) = \varepsilon_g + \alpha \cdot \frac{t}{t_e} \tag{23}$$

where ε_g is the uniform strain, $\alpha = \varepsilon_m \cdot (x_e/t)$ is a factor that depends on the necking strain and the length of the neck, t is the thickness of the plate, and l_e is the length of the individual elements. The recommendation is that the l_e/t ratio not be less than 5 for shell elements. For plate thickness of 5 mm, $\varepsilon_g = 0.1$ and $\alpha = 0.8$. For plate thickness between 12.5 and 20 mm, $\varepsilon_g = 0.08$ and $\alpha = 0.65$. As noted in [8], an elastic-plastic material with isotropic strain hardening was used to obtain these values. The type of material was normal shipbuilding steel and austenitic steel with material code nos. 1.4404 and 1.4306. Previous studies that used the Peschmann criterion are listed in Table 2.

2.6.3 Rice-Tracey and Cockcroft-Latham criterion

The Rice-Tracey and Cockcroft-Latham (RTCL) criterion was developed by Törnqvist [20]. The Rice and Tracey criterion is based on void growth and coalescence. The Cockcroft-Latham criterion corresponds to failure by shear under small stress triaxiality. These two damage models cover the full range of stress triaxiality. The RTCL formulation yields:

$$D = \int \frac{\sigma_1}{\sigma_e} d\varepsilon_e \quad \text{if } -0.33 < T < 0.33, \tag{24}$$

$$D = \int \frac{1}{C} exp\left(\frac{3\sigma_m}{3\sigma_e}\right) d\varepsilon_e \quad \text{if } T > 0.33, \tag{25}$$

The mesh sensitivity is described by the following expression:

$$D_{cr}\left(\frac{t}{l_e}, T = 0.33\right) = \varepsilon_f\left(\frac{t}{l_e}\right) = n + (\varepsilon_n - n)\frac{t}{l_e} \tag{26}$$

where n is the power-law exponent and diffuse necking strain, and ε_n is the failure strain at $t/l = 1$ at uniaxial stress. These values are equal to $n = 0.205$ and $\varepsilon_n = 0.67$, which were obtained using steel [18] with a density of 7850 kg/m^3, Young's Modulus of 206 MPa, and a Poisson ratio of 0.3. For a yield stress value of 284 MPa, the strength coefficient is

Table 3: Research that used the Rice-Tracey and Cockcroft-Latham criterion

No.	Research title	Methodology	Author	Year
1	Simulating the collision response of ship side structures: A failure criteria benchmark study	FE analysis	Ehlers *et al.* [18]	2008
2	Crashworthiness assessment of thin-walled bottom structures during powered-hard grounding accidents	FE analysis	Prabowo *et al.* [19]	2018
3	Benchmark study of failure criteria for ship collision modeling using purpose-designed tensile specimen geometries	Experiment and FE analysis	Calle *et al.* [2]	2017a

$K = 730$, and the strain-hardening index is $n = 0.20$. Previous studies that used the Rice-Tracey and Cockcroft-Latham criterion are listed in Table 3.

2.6.4 Ultimate strain criterion

The ultimate strain criterion assumes that the structure will fail due to maximum elongation. This elongation reaches a critical strain due to excessive load, causing the structure to fail. In mathematical form, this criterion can be written as:

$$\varepsilon_{max} = \varepsilon_c \tag{27}$$

McDermott *et al.* [48] defined the critical strain for mild steel as:

$$\varepsilon_c = 0.10 \cdot \left(\frac{\varepsilon_f}{0.32}\right) \tag{28}$$

where ε_f is the tensile ductility. The tensile ductility of mild steel has experimental values ranging from 0.20 to 0.35. However, due to scale effects and material imperfections, this value is far too large to be used. Amdahl [25] suggested that the critical strain value is between 5% and 10%. This failure criterion was previously used by Zhang [26].

3 Benchmarking based on pioneering experiments

In this study, several laboratory tensile test experiments were reconducted with the finite element program as validation. Validation through experiments is essential because the accuracy of simulation results can be significantly affected by several major parameters in the finite element program. The details of the experiments and the properties of the tested materials are introduced in the next sections.

3.1 Experimental validation based on Wang et al. [45]

For the validation study in the current work, the laboratory tensile test reported by Wang *et al.* [45] was reconducted. The dimensions of the tensile test specimen are shown in Figure 5. The standard dimensions of the specimen are an overall length of 200 mm, grip section length of 50 mm, grip section width of 45 mm, and fillet radius of 25 mm. The width and the length of the reduced section are 20 mm and 75 mm, respectively. The material for the tensile test is mild steel with the material properties listed in Table 4. The material has a density of 7850 kg/m^3, Young's modulus of 201 GPa, and a Poisson ratio of 0.3.

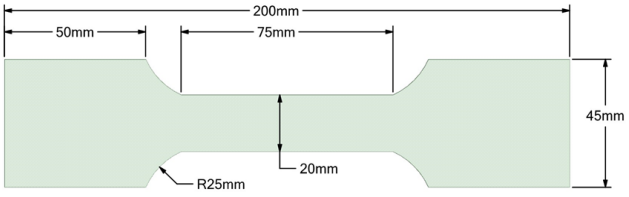

Figure 5: The dimensions of the tensile test specimen

Table 4: Basic mechanical properties of mild steel

Properties	Unit	Value
Material density	kg/m^3	7850
Young's modulus	GPa	201
Ultimate tensile strength	MPa	361
Yield stress	MPa	245
Poisson ratio	-	0.3

The tensile test model was established using solid (SOLID186), and shell (SHELL181) element types; mesh sizes of 2.5 mm × 2.5 mm, 5 mm × 5 mm, 7.5 mm × 7.5 mm, and 10 mm × 10 mm were used for each element type. A solid

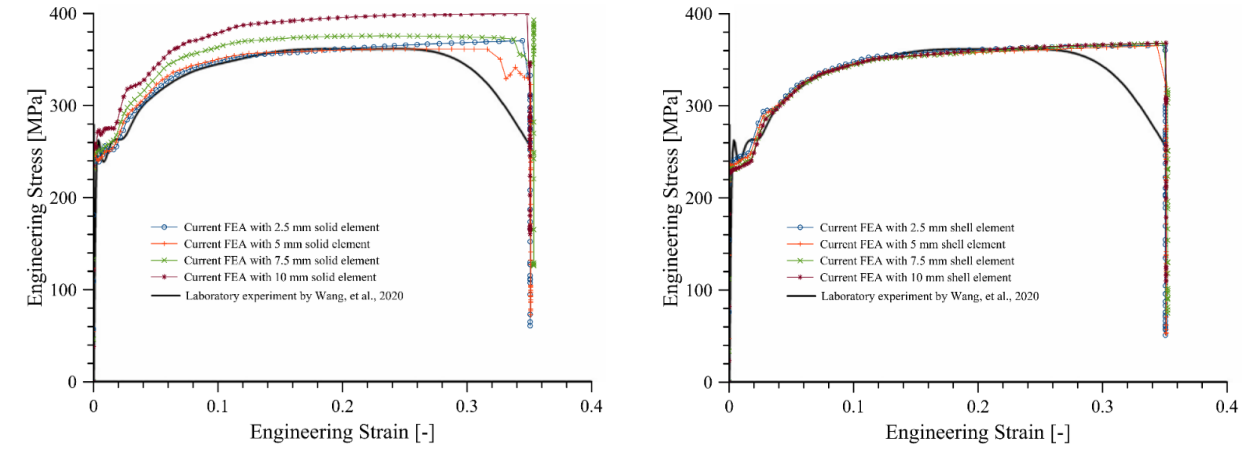

(a) (b)

Figure 6: Comparison of engineering stress-strain curves from the current numerical simulation and experimental tensile test: (a) with the solid element type; (b) with the shell element type

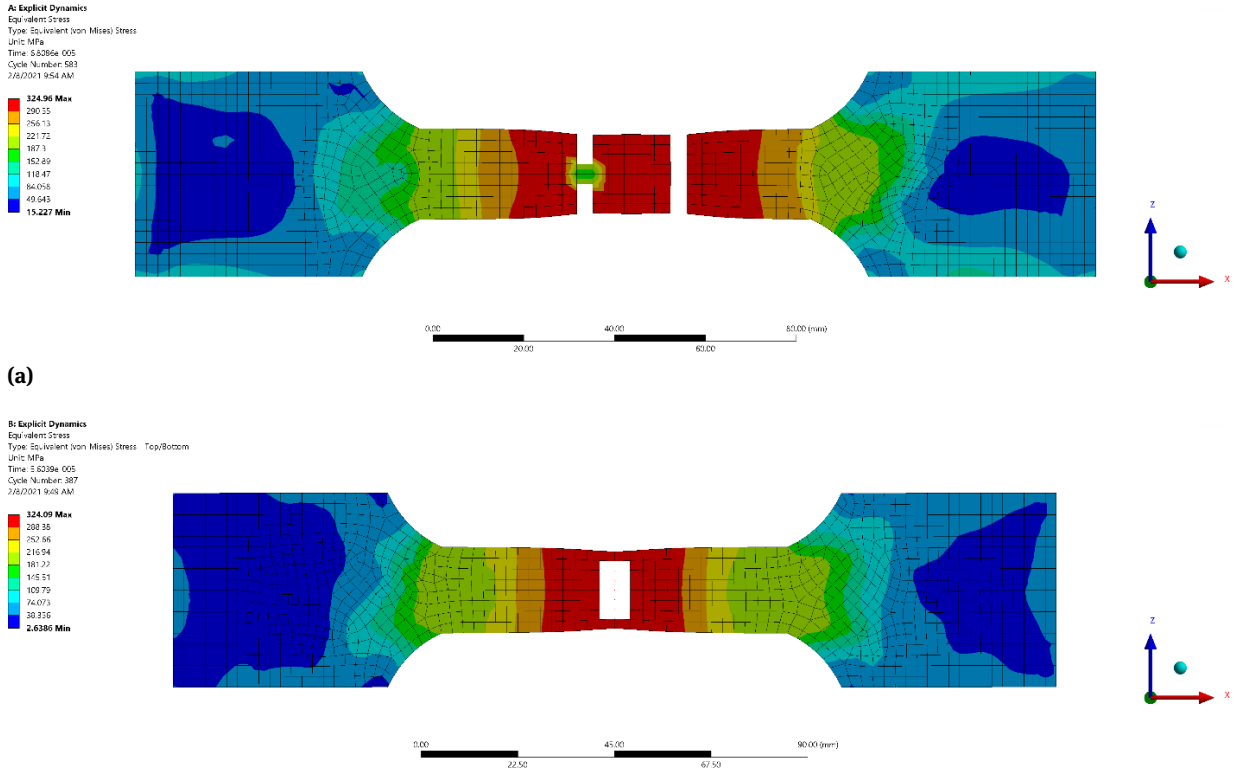

(a)

(b)

Figure 7: The von Mises stress and localized necking in the specimen: (a) with the solid element type; (b) with the shell element type

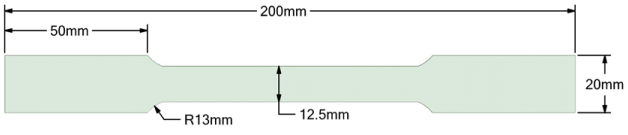

Figure 8: The dimensions of the tensile test specimen

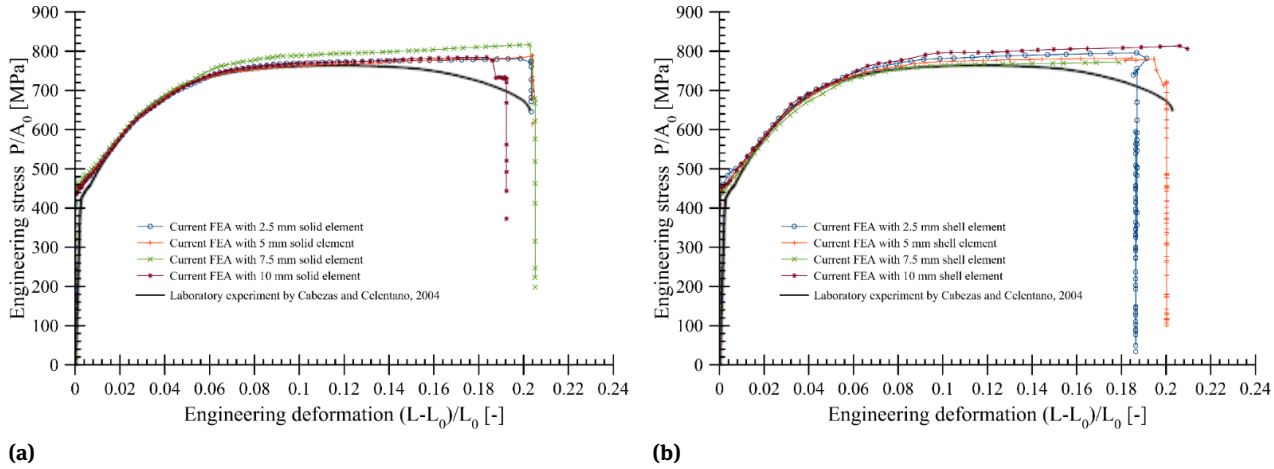

Figure 9: Comparison of engineering stress-strain curves from the current numerical simulation and experimental tensile test: (a) with the solid element type; (b) with the shell element type

model is a solid element where the material is represented throughout the component/structure (3D). SOLID186 is a higher-order 3-D 20-node solid element that exhibits quadratic displacement behavior. The element is defined by 20 nodes having three degrees of freedom per node: translations in the nodal x, y, and z directions. Moreover, shell elements do not consider the stress in the direction perpendicular to the shell surface (2D). SHELL181 is suitable for analyzing thin to moderately-thick shell structures. It is a four-node element with six degrees of freedom at each node: translations in the x, y, and z directions, and rotations about the x, y, and z-axes. For the boundary condition, each grip section of the specimen was pulled by forces in the opposite direction until a fracture occurred. The numerical simulation was carried out for 1×10^{-4} seconds. The results of the current simulation and the experimental test are shown in Figure 6. As shown in the figure, the stress-strain curves obtained from the simulation with both the solid and shell element types are consistent with the experimental results. However, slightly higher ultimate tensile strength is observed when the 7.5 mm and 10 mm solid elements are used. These two solid elements result in ultimate tensile strengths of 375 MPa and 400 MPa, respectively, compared with the experimental result of 361 MPa. On the other hand, the results of all numerical simulations with the shell element types are consistent with the experimental values. Figure 7 shows the distribution of von Mises stress in the specimen with both the solid and shell element types after a fracture occurs. The von Mises stress contour shows that the highest stress is experienced in the middle of the gauge length, which means that the damage and the maximum stress are mainly concentrated in this region. This area experiences a high stress concentration, which causes the necking phenomenon, and is ultimately the point of fracture in the specimen.

3.2 Experimental validation based on Cabezas and Celentano [49]

The experimental tensile test performed by Cabezas and Celentano [49] was reconducted with the finite element program. The material used in the experimental test is SAE 1045 steel. Table 5 lists the average chemical composition of SAE 1045 steel, which has an elemental composition of 0.447% Carbon (C) and 0.756% Manganese (Mn) by weight. The tensile test specimen in the experiment has standard ASTM standard dimensions, as depicted in Figure 8. The standard dimensions of the specimen are an overall length

Table 5: Average chemical composition and the percentage of SAE 1045 steel (% in weight)

C	Si	Mn	P	S
0.447	0.213	0.756	0.0148	0.03272
Cr	Mo	Ni	Al	Cu
0.0635	0.0139	0.0914	<0.00106	0.277
Nb	Ti	V	W	Pb
<0.0050	0.00219	0.00917	<0.01	<0.005
Sn	B	Fe	Co	
0.0159	<0.00051	98.02	0.0172	

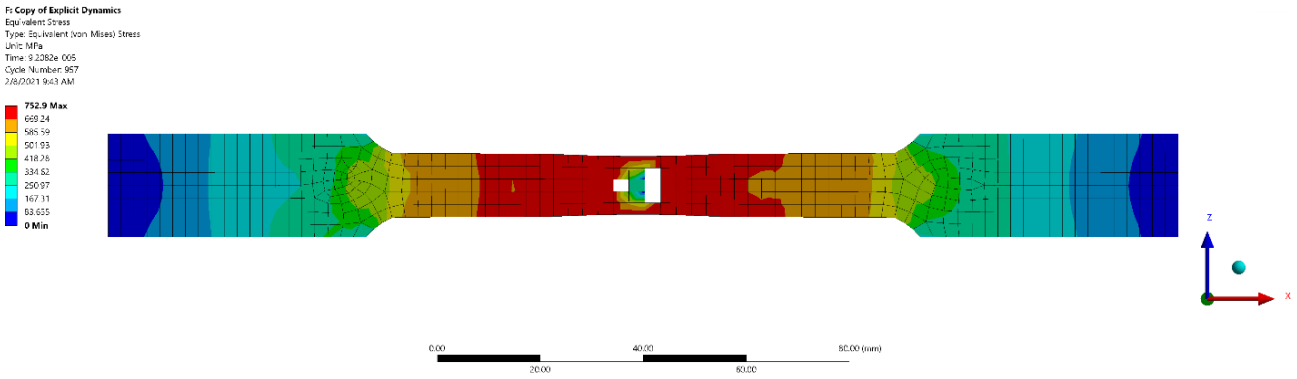

(a)

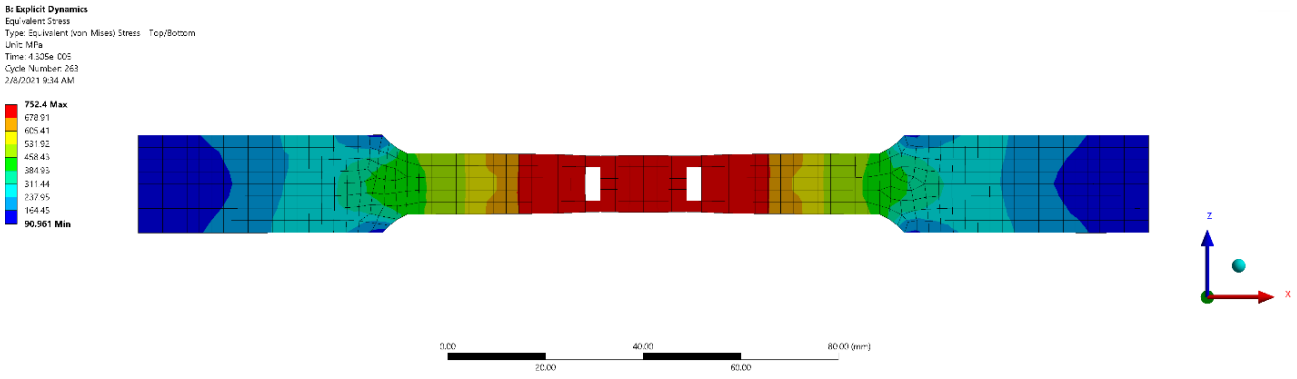

(b)

Figure 10: The von Mises stress and localized necking in the specimen: (a) with the solid element type; (b) with the shell element type

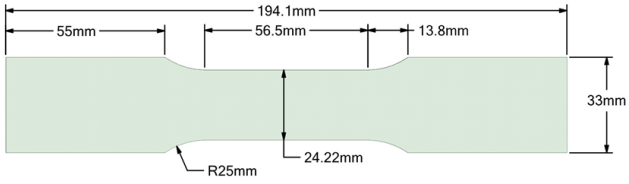

Figure 11: The dimensions of the tensile test specimen

Table 6: Material properties from Wiegard and Ehlers [50]

Properties	Unit	Value
Material density	kg/m^3	7800
Young's modulus	GPa	210
Yield stress	MPa	349
Poisson ratio	-	0.3
Failure strain	-	0.89

of 200 mm, grip section length of 50 mm, grip section width of 20 mm, and fillet radius of 13 mm. The width of the gauge length is 12.5 mm.

The boundary conditions are the same as described in Section 3.1. The results of the current simulation and the experimental test are shown in Figure 9. The figure shows that the stress-strain curves obtained from the simulation with both the solid and shell element types are in good agreement with the experimental result. The maximum engineering stress is observed at 762 MPa in the experiment and 780 MPa and 795 MPa in the tensile test simulation when 2.5 mm solid and shell elements are used, respectively. Figure 10 shows the distribution of von Mises stress with both the solid and shell element types in the specimen after a fracture occurs. In the gauge length region, the necking phenomenon appears at the point where the fracture occurs.

3.3 Experimental validation based on Wiegard and Ehlers [50]

The tensile test performed by Wiegard and Ehlers [50] was reconducted. The dimensions of the test specimen are presented in Figure 11. The specimen has a length of 194.1 mm, grip section length of 55 mm, grip section width of 33 mm, and fillet radius of 25 mm. The width of the gauge length is 24.22 mm. The material used in the test has a density of 7800 kg/m^3, Young's modulus of 210 GPa, and a Pois-

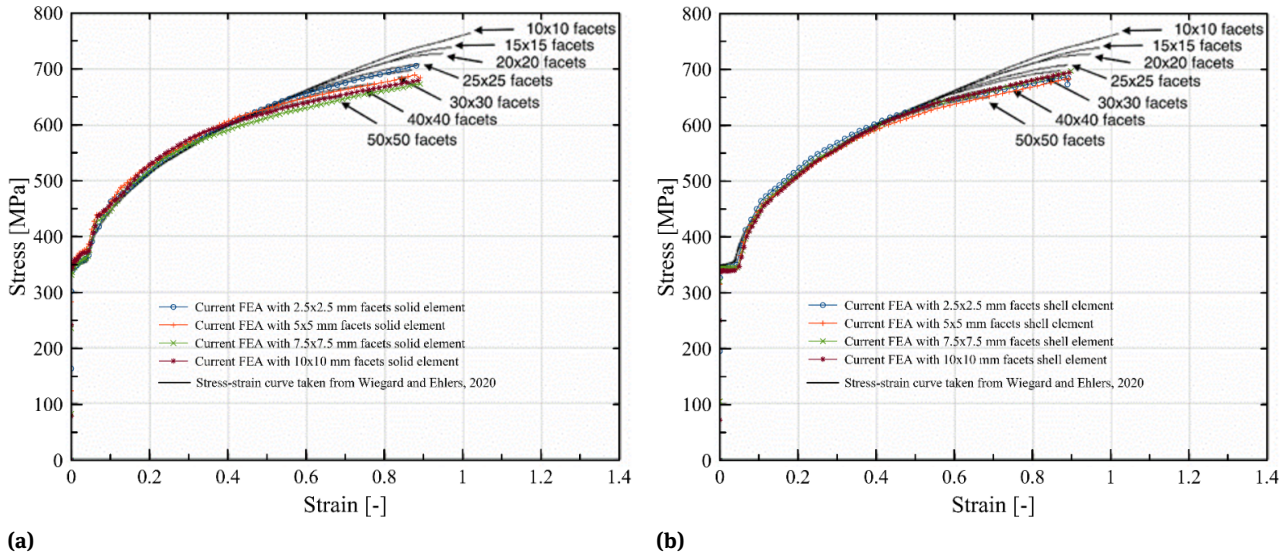

Figure 12: Comparison of engineering stress-strain curves from the current numerical simulation and experimental tensile test: (a) with the solid element type; (b) with the shell element type

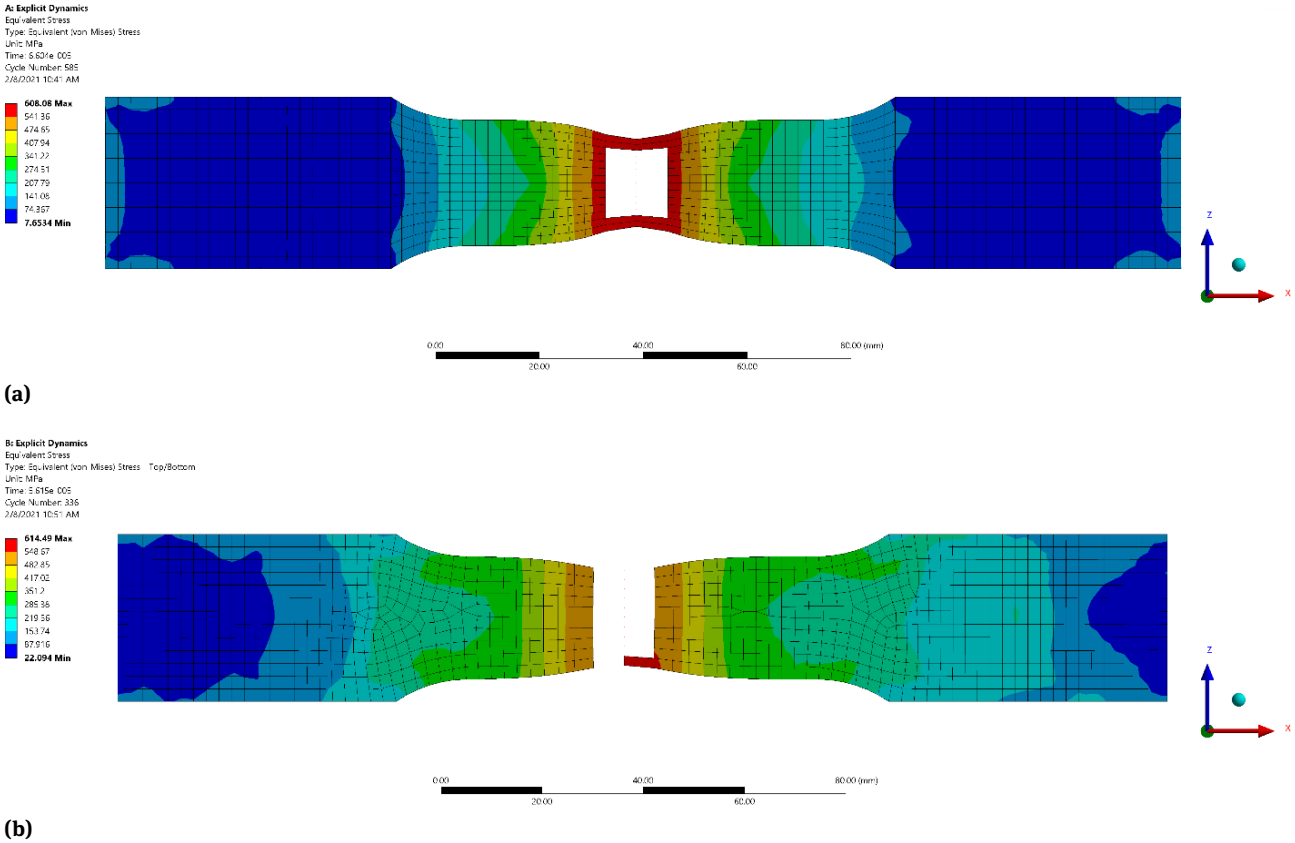

Figure 13: The von Mises stress and localized necking in the specimen: (a) with the solid element type; (b) with the shell element type

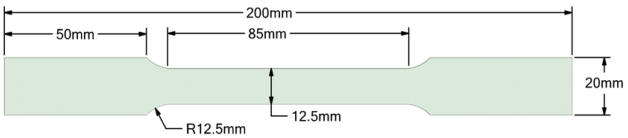

Figure 14: The dimensions of the tensile test specimen

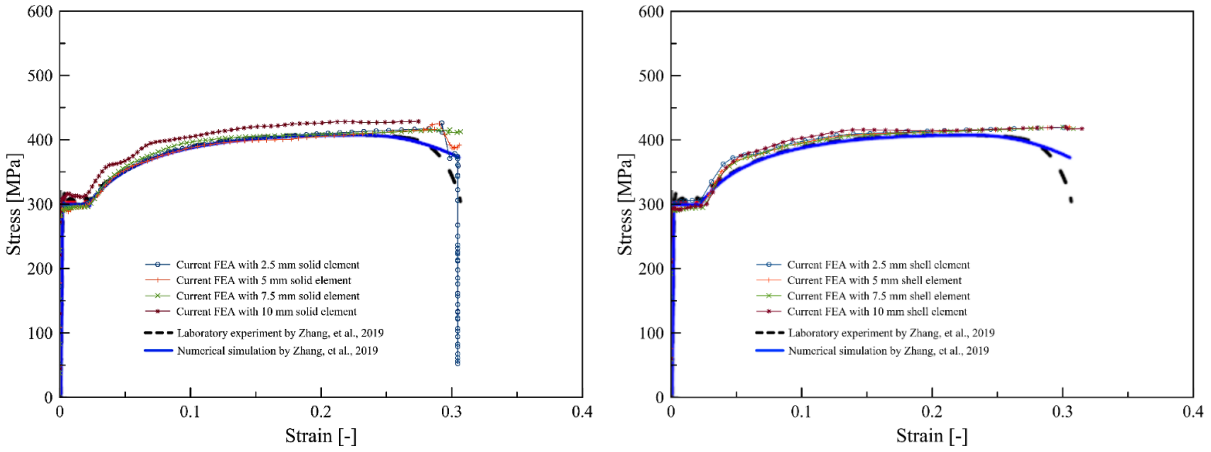

Figure 15: Comparison of engineering stress-strain curves from the current numerical simulation and experimental tensile test: (a) with the solid element type; (b) with the shell element type

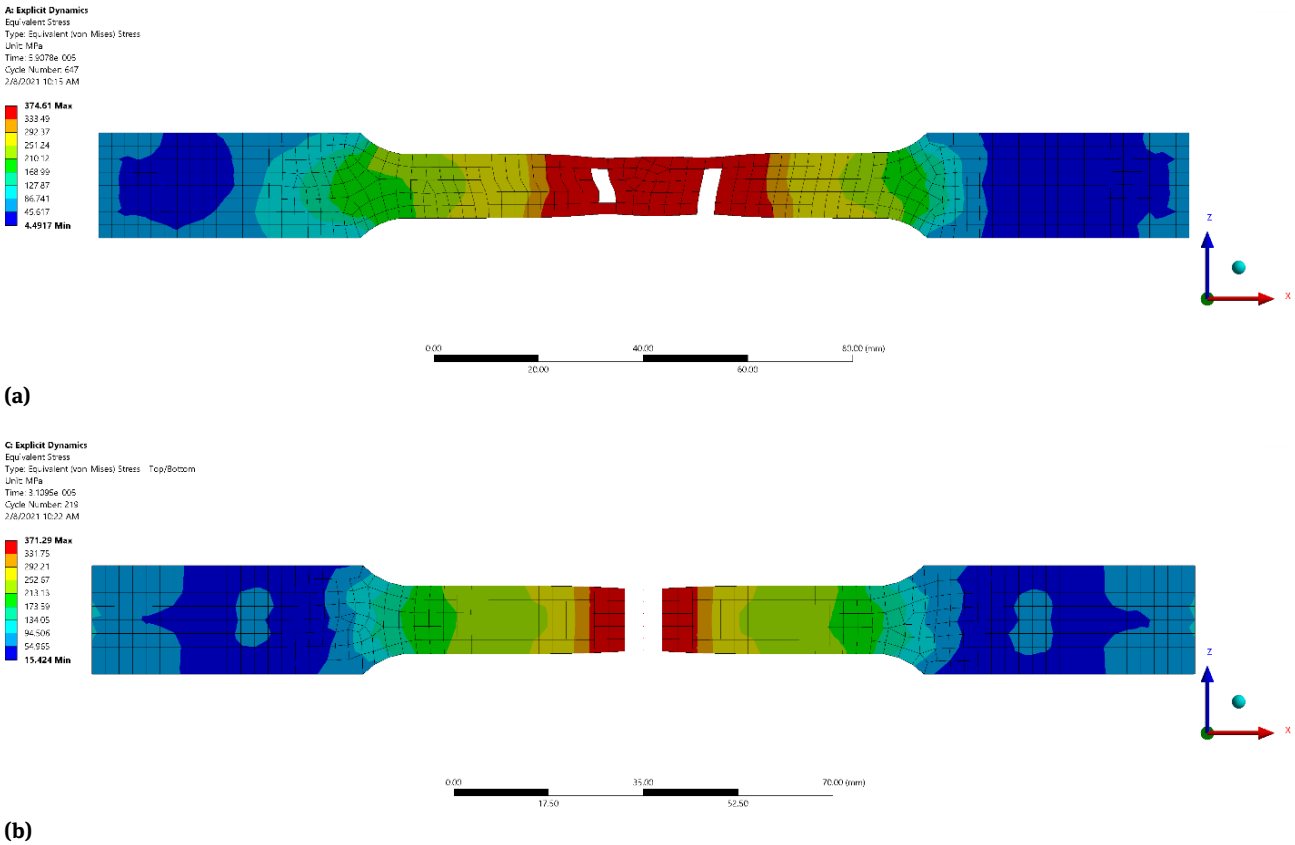

Figure 16: The von Mises stress and localized necking in the specimen: (a) with the solid element type; (b) with the shell element type

Table 7: Mechanical properties of the material [51]

Properties	Unit	Value
Material density	kg/m^3	7850
Young's modulus	GPa	207
Ultimate tensile strength	MPa	408.4
Yield stress	MPa	302.8
Poisson ratio	-	0.3
Failure strain	-	0.306
Strength coefficient	MPa	690.2
Strain-hardening index	-	0.2
ε_{plat}	-	0.0189

son ratio of 0.3. The details of the material are described in Table 6.

The boundary conditions used are the same as described in Section 3.1. As shown in Figure 12, the stress-strain curves obtained in the numerical simulation and experiments show reasonable agreement. The stress is almost the same as the experimental result. Figure 13 shows the distribution of von Mises stress with both the solid and shell element types in the specimen after a fracture occurs.

3.4 Experimental validation based on Zhang et al. [51]

The next validation was performed by reconducting the laboratory tensile test reported by Zhang *et al.* [51]. The material has a density of 7850 kg/m^3, Young's modulus of 207 GPa, and a Poisson ratio of 0.3. The mechanical properties of the material are summarized in Table 7. The tensile test was conducted using standard tensile specimens and procedures and performed on a universal testing machine. The dimensions of the test specimen are an overall length of 200 mm, gauge length of 85 mm, grip section width of 20 mm, and fillet radius of 12.5 mm. The dimensions of the standard tensile test specimen are shown in Figure 14.

For the boundary condition, the same test setup as in Section 3.1 was employed. The engineering stress-strain curves obtained from the experimental test and the finite element simulations are shown in Figure 15. A reasonable agreement with the experimental results is observed. However, the simulation result shows a slightly higher ultimate tensile strength of 428 MPa when a 10 mm solid element is used compared with the experimental result of 408.4 MPa. Thus, the simulation result is 19.6 MPa higher than the experimental value. On the other hand, relatively good agreement with the experimental result is achieved when the shell element type is used. The von Mises stress obtained in the numerical simulation is shown in Figure 16, and localized necking can be seen in the gauge length where the fracture occurs.

3.5 Experimental validation based on Calle et al. [2]

For the fifth validation, the experimental tensile test conducted by Calle *et al.* [2] was reconducted. The material in the experiment is a cold-rolled SAE 1008 carbon steel sheet with a thickness of 0.25 mm and is considered to be equivalent to the Grade A naval steel plates (25 mm thickness) normally used in the shipbuilding industry. The material has a density of 7800 kg/m^3, Young's modulus of 205 GPa, and a Poisson ratio of 0.3. The mechanical properties of the material are summarized in Table 8. The experiment was performed with uniaxial tensile tests using an Instron universal testing machine, model 3369, with a clamp velocity of 0.0025 mm/s. The tensile test used a standard specimen, and the dimensions are shown in Figure 17. The specimen dimensions are an overall length of 150 mm, grip section length of 40 mm, grip section width of 25 mm, and fillet radius of 10.4 mm.

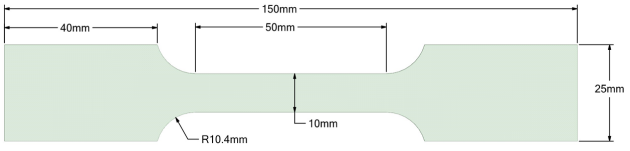

Figure 17: The dimensions of the tensile test specimen

Table 8: The mechanical properties of the material

Properties	Symbol	Unit	Value
Material density	ρ	kg/m^3	7800
Young's modulus	E	GPa	205
Poisson ratio	v	-	0.3
UTT failure criterion parameters	ε_n	-	0.2674
	ε_u	-	0.5071

The boundary conditions described in Section 3.1 were applied to this test. The engineering stress-strain curves obtained from the experimental test and the finite element simulations are shown in Figure 18. The figure shows that the fifth validation model achieves reasonable agreement with the experimental results. A higher ultimate tensile

strength is observed when the 7.5 mm and 10 mm solid elements are used. These two solid elements produce ultimate tensile strengths of 422 MPa and 417 MPa, respectively, compared with the experimental value of about 370 MPa. Thus, the simulation results are about 52 MPa and 47 MPa higher than the experimental value. With the shell elements, relatively good agreement with the experimental result is achieved. The von Mises stress from the simulation is shown in Figure 19, and localized necking can be seen in the gauge length where the fracture occurs.

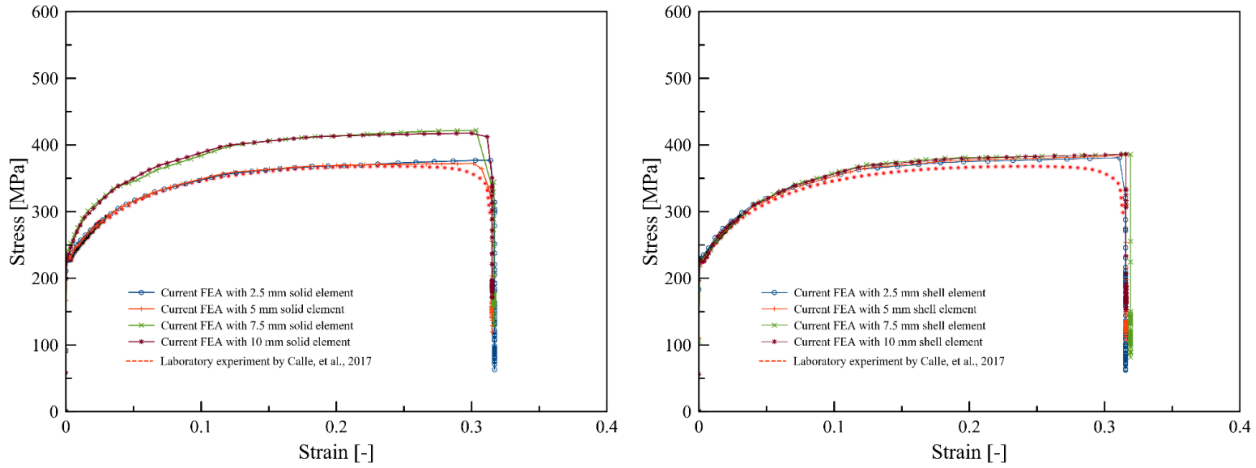

(a) (b)

Figure 18: Comparison of engineering stress-strain curves from the current numerical simulation and experimental tensile test: (a) with the solid element type; (b) with the shell element type

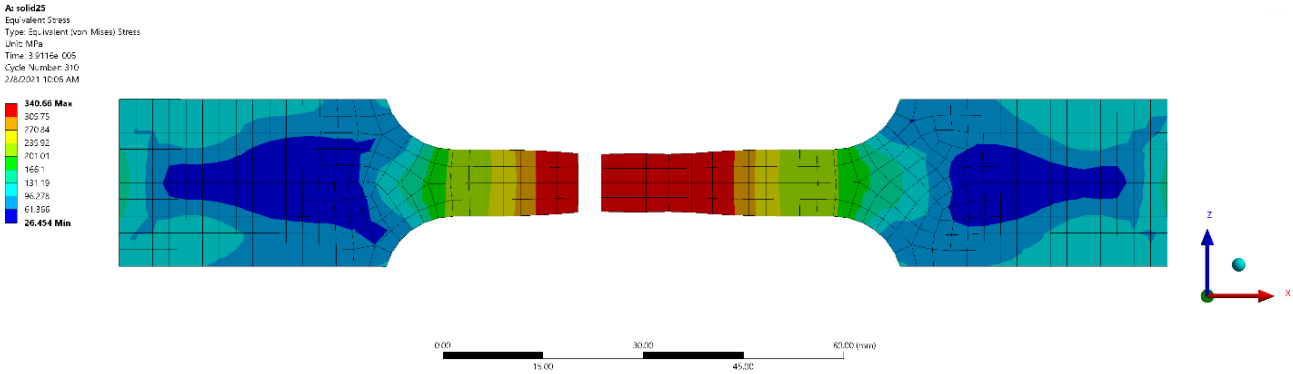

(a)

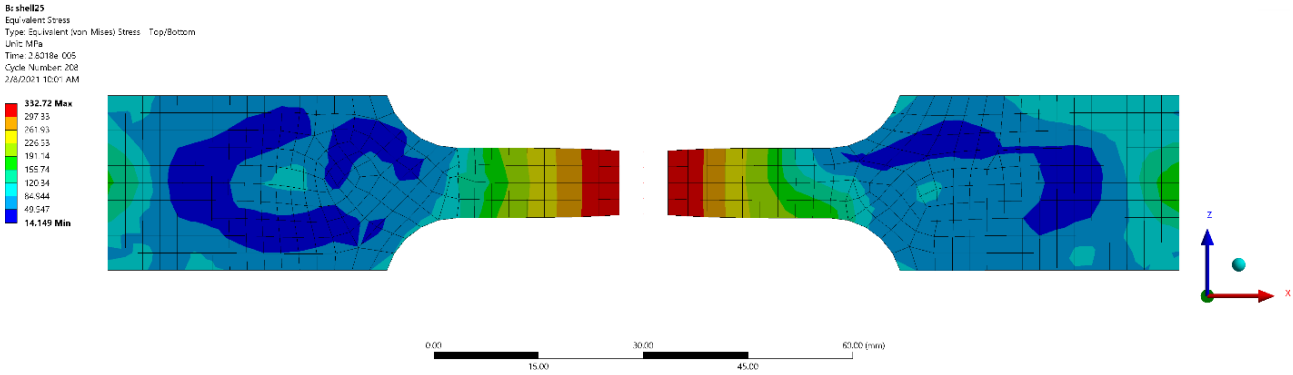

(b)

Figure 19: The von Mises stress and localized necking in the specimen: (a) with the solid element type; (b) with the shell element type

Table 9: Material properties of the investigated steels

Material	Steel grade	Density [kg/m^3]	Young's modulus [GPa]	Yield strength [MPa]	Ultimate strength [MPa]	Poisson's ratio
Medium-carbon steel	1030	7850	206	345	550	0.29
High-carbon steel	1080	7850	205	585	965	0.29
High-strength low-alloy (HSLA)	A606	7750	205	310	448	0.28

4 Extended study: failure behaviors under tensile loads

4.1 Technical geometry

The specimens used in this study have four different geometries, as shown in Figure 20. Specimens 1 and 2, shown in Figures 20a and 20b, were previously used in the numerical analysis of ship collision and grounding by Calle *et al.* [2, 41]. The experiments included scaled collision tests of a T cross-section beam, head-on collision of an oil tanker against a rigid wall, ship grounding, and collision between two oil tankers.

The tensile specimen lengths are 150 mm and 59 mm, and the widths of the lengths of the reduced sections are 10 mm and 4 mm, respectively. Both specimens have a grip section width of 25 mm. Reference specimens 3 and 4 are from Iannucci *et al.* [52], who studied the effect of thickness on the tensile strength of Dyneema®HB26 laminates, and from Törnqvist [20], who explored the design of crashworthy ship structures, respectively. The specimens have lengths of 300 mm and 210 mm, and the widths of the lengths of the reduced section are 10 mm and 30 mm, respectively. Both specimens have a grip section width of 50 mm. The dimensions of all specimens are shown in Figure 20.

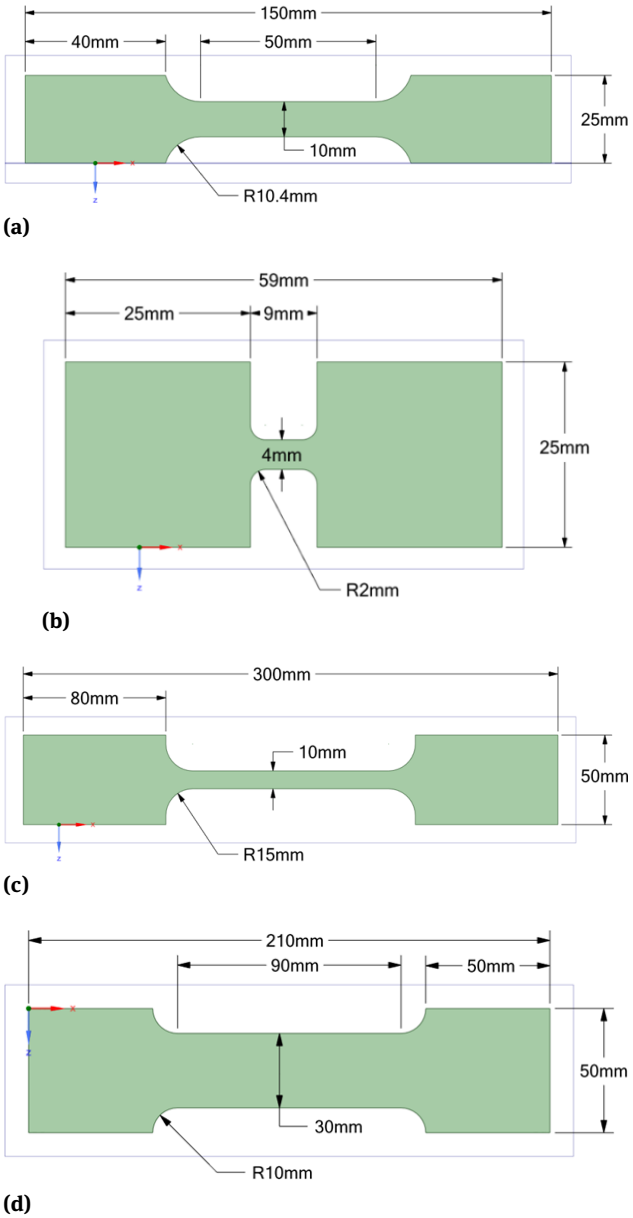

Figure 20: Tensile test specimens with rectangular cross-section: (a) tensile test specimen 1; (b) tensile test specimen 2; (c) tensile test specimen 3; (d) tensile test specimen 4

4.2 Applied material and failure criterion

The ultimate strain criterion and three failure criteria, i.e., the Germanischer Lloyd (GL) [16], Peschmann [17], and Rice-Tracey and Cockcroft-Latham (RTCL) criteria, were used in this investigation [20]. Different failure criteria were applied in the numerical tensile test with different materials. The material properties of the investigated steel materials are listed in Table 9. The materials are medium-carbon steel 1030, high-carbon steel 1080, and HSLA A606, and their densities are 7850 kg/m^3, 7850 kg/m^3, and 7750 kg/m^3, respectively.

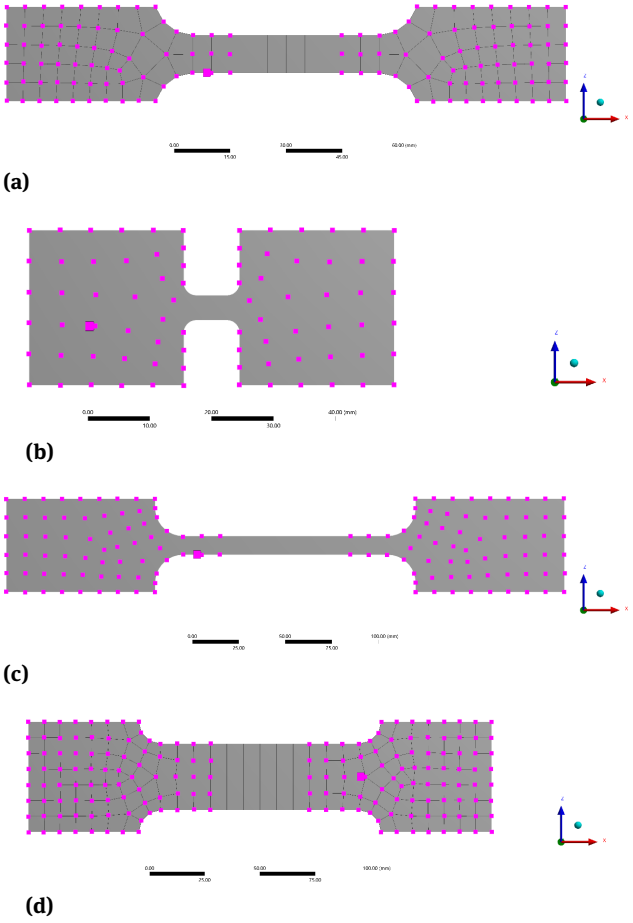

Figure 21: The clamping areas in the specimens are indicated by the square pattern in magenta: (a) specimen 1; (b) specimen 2; (c) specimen 3; (d) specimen 4

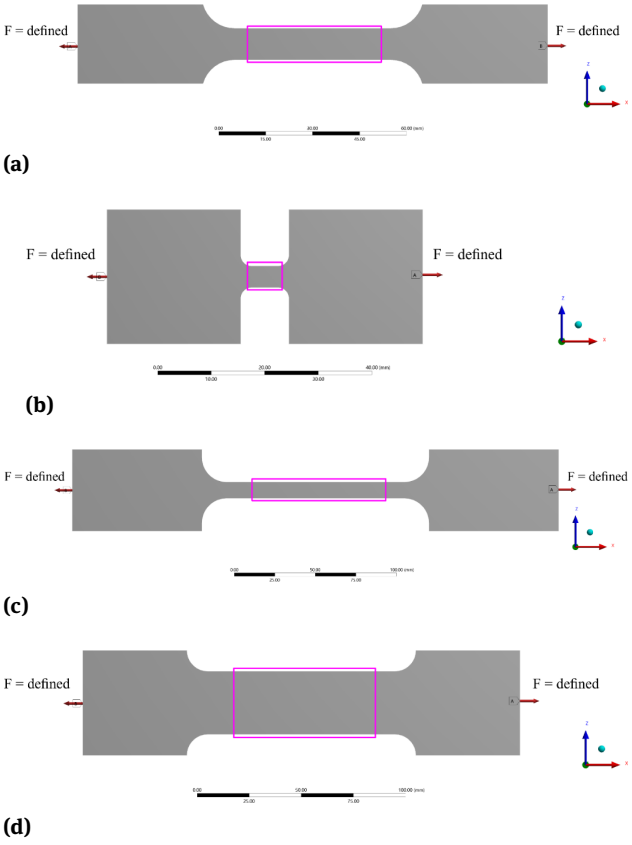

Figure 22: The tensile test analysis and boundary condition of the proposed models: (a) specimen 1; (b) specimen 2; (c) specimen 3; (d) specimen 4

Two of these failure criteria, the Peschmann and Rice-Tracey and Cockcroft-Latham criteria, were studied in great detail in the Master of Science thesis by Odefey [53].

4.3 Scenario and boundary conditions

The numerical tensile test consisted of opposite axial nodal forces acting on both sides of the specimen until a fracture occurred. During the tests, clamping areas in the specimen were placed near the end of the gauge length on both side surfaces. Clamping areas in the specimens are indicated by the square patterns in magenta in Figure 21. During the tensile test analysis, boundary conditions (Figure 22) were applied.

Nodal forces on the clamps, as shown in Figure 21, were applied in opposite directions, as indicated by the arrows in Figure 22. When selecting the nodes on which the nodal forces act, the box volume selection was used. The magenta outline in Figure 22 indicates the region in which the failure was analyzed. During every tensile test simulation, the time was set to 1×10^{-4} s. The environmental temperature was set to 22°C. The tensile test was terminated when the specimen failed to retain the load. To produce a variety of results, meshing sizes of 2.5, 5, 7.5, and 10 mm were used for the specimens. The automatic method was used when implementing the mesh size on the specimens. In addition, when sizing the mesh relative to the body of the specimens, the element size type was used. In the output data, the equivalent plastic strain and normal stress are plotted on the x- and y-axes, respectively.

5 Effects of physical and numerical parameters

The simulation result regarding the effect of modeling parameters is presented. The influence of specimen topology of obtained characteristic results under three failure criteria, including GL, Peschmann, and RTCL, is explained in detail.

5.1 Specimen topology

The effect of four different specimen topologies with different mesh sizes is investigated to obtain the stress-strain characteristic under different failure criteria. Total of four different specimens with different topologies were examined. The stress-strain curve for each specimen with the Germanischer Lloyd (GL) criterion and AISI 1030 steel is presented in Figure 23. Figure 23 shows the engineering stress-strain for the four specimen models. As shown in the figure, there are fairly large differences in the maximum strain ε_f for specimen 2 compared with the three other specimens. The rupture in specimen 2, which has the shortest gauge length of the specimens, occurs earlier compared with the other specimens when mesh size l_e = 5 mm, 7.5 mm, and 10 mm, as shown in Figure 23b. With these mesh sizes, the rupture strain is 0.12, 0.10, and 0.08, respectively. Only the 2.5 mm mesh size of specimen 2 has a rupture strain with the same tendency as the other three specimens. The rupture strain obtained with this mesh size is 0.27. On the other hand, the other three specimen topologies, i.e., specimens 1, 3, and 4, have identical tendencies and reasonable agreement.

The results show that specimens 1, 3, and 4 are able to effectively predict fracture initiation for various failure criteria. Furthermore, these three specimens can produce the same results and tendencies for all proposed lengths of the element l_e. As shown in Figure 23, the initial positions of the rupture strain of specimens 1, 3, and 4 are at ε_f = 0.27, 0.16, 0.12, and 0.11 with mesh size l_e = 2.5 mm, 5 mm,

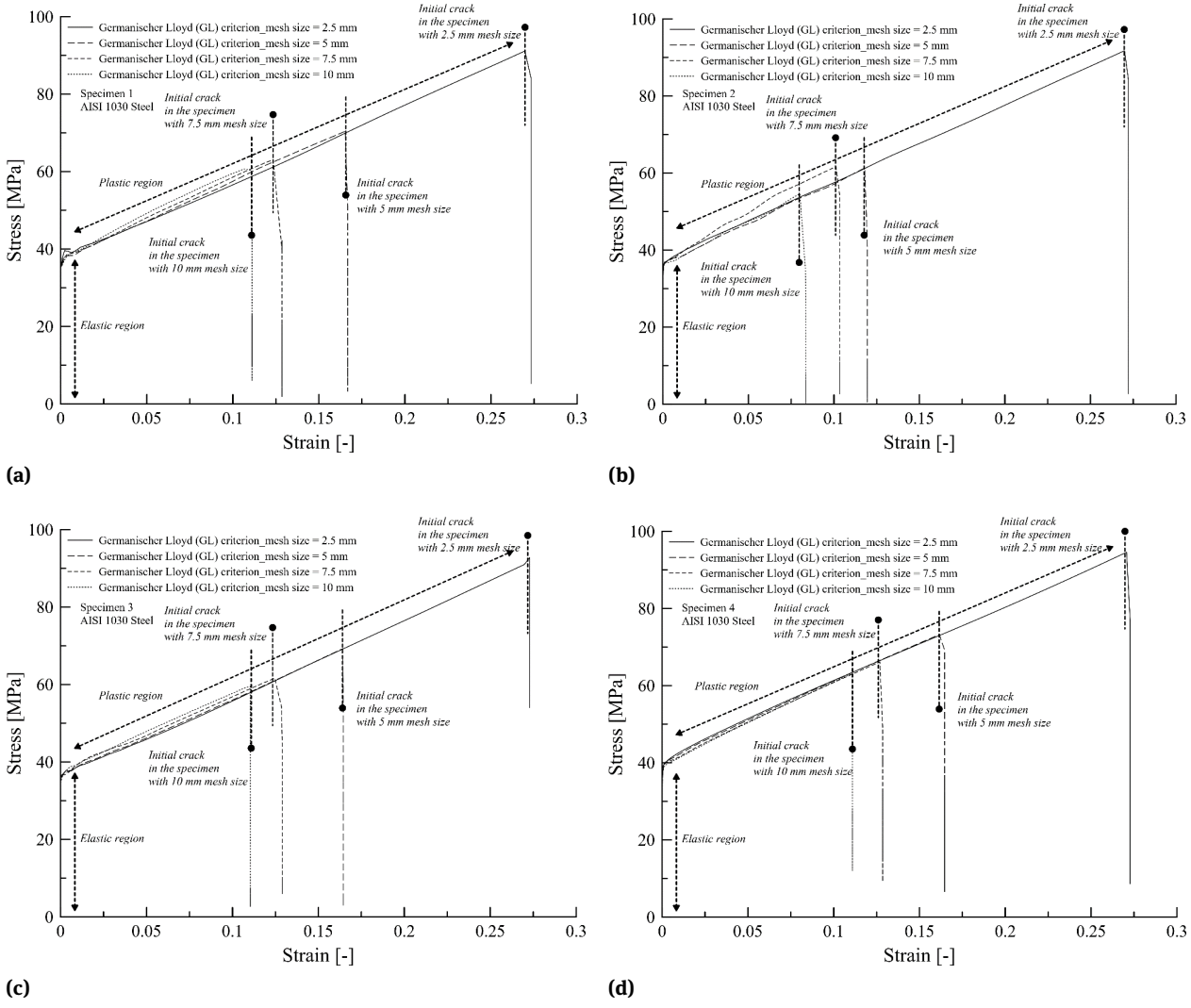

Figure 23: The stress-strain curve with Germanischer Lloyd (GL) criterion and AISI 1030 steel: (a) specimen 1; (b) specimen 2; (c) specimen 3; (d) specimen 4

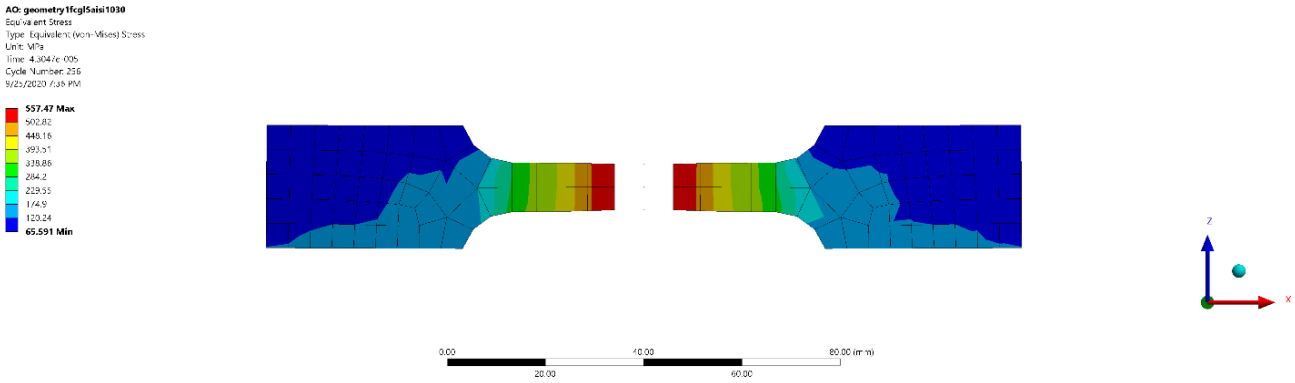

(a)

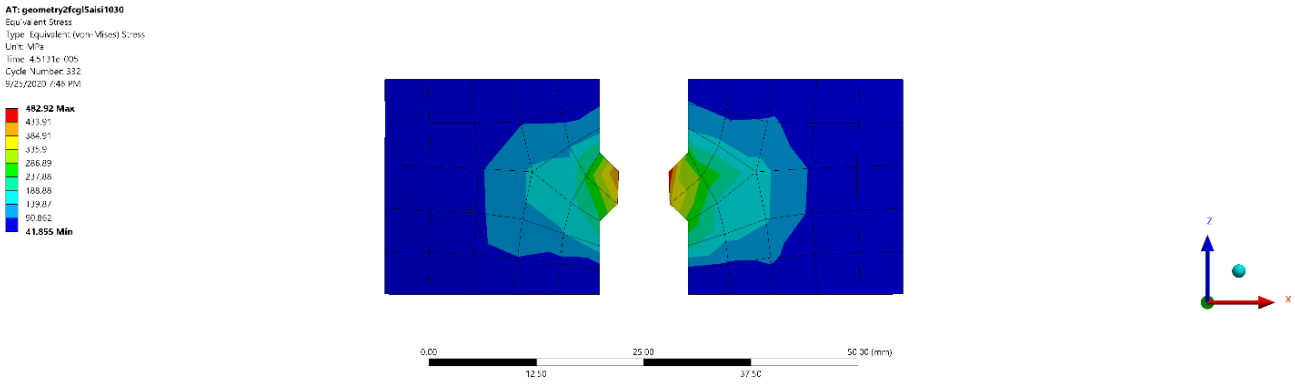

(b)

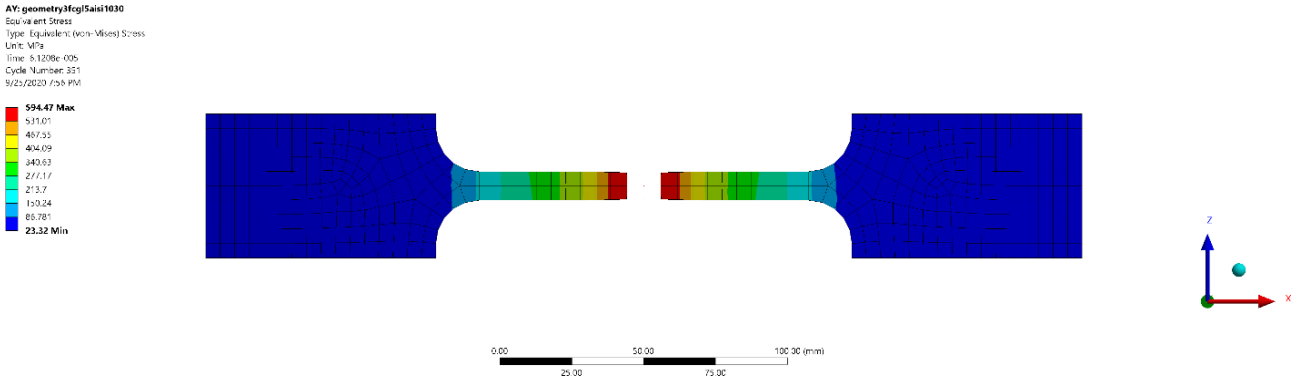

(c)

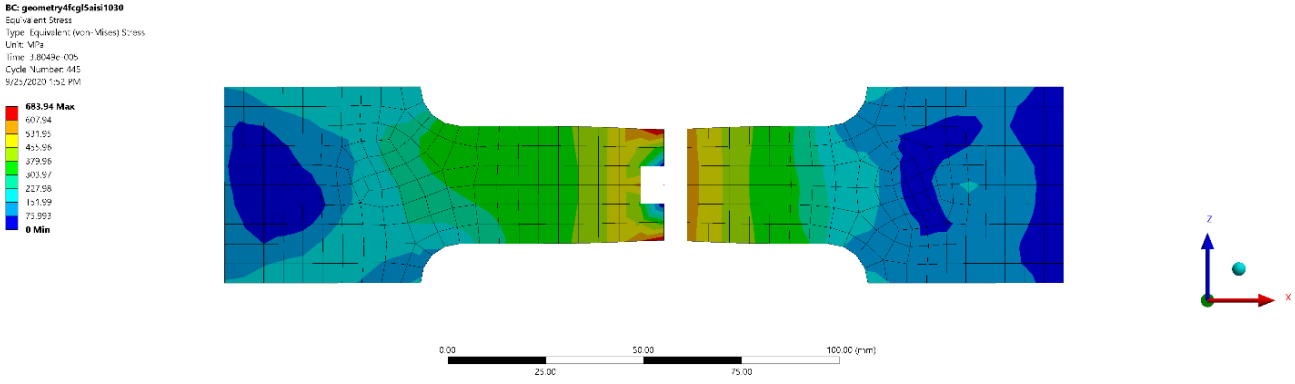

(d)

Figure 24: The von Mises stress distribution in the specimen after a fracture occurs with 5 mm mesh size and the Germanischer Lloyd (GL) criterion: (a) specimen 1; (b) specimen 2; (c) specimen 3; (d) specimen 4

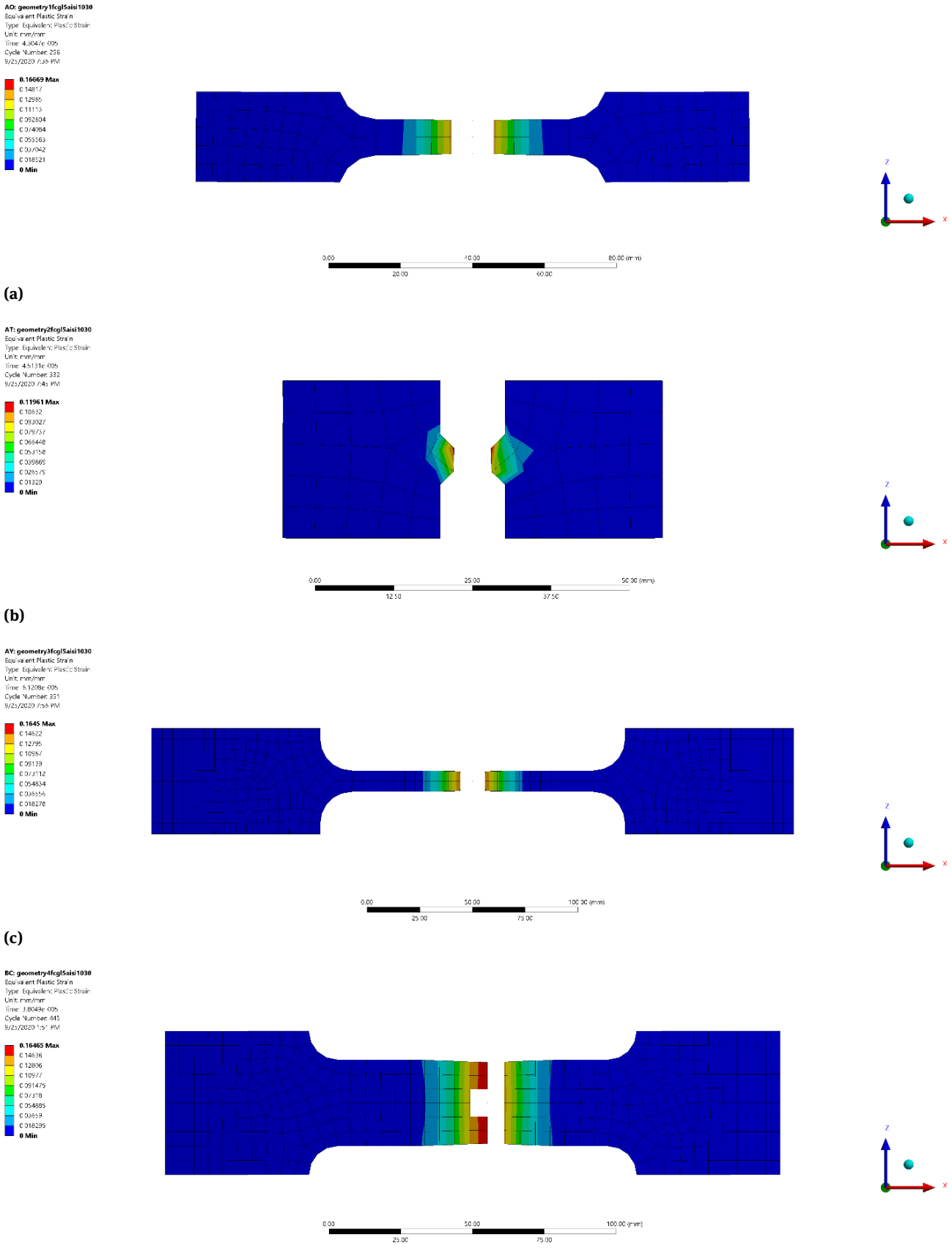

Figure 25: The maximum strain distribution in the tensile test after a fracture occurs with 5 mm mesh size and the Germanischer Lloyd (GL) criterion: (a) specimen 1; (b) specimen 2; (c) specimen 3; (d) specimen 4

7.5 mm, and 10 mm, respectively. These specimens also produce almost identical engineering stress-strain curves.

The von Mises stress and the strain [54, 55] contours of the four specimen topologies after the failure occurs are presented in Figures 24 and 25, respectively. In Figure 25b, the strain contour for specimen 2 with l_e = 5 mm mesh size is presented. As observed in the figure, there are fairly large differences in the location of the maximum strain contour compared with the other three specimen topologies, as shown in Figure 25a, 25c, and 25d. The grip section near the gauge length of specimen 2 experiences a slight strain phenomenon when a mesh size greater than 2.5 mm is used. This tendency is observed in specimen 2 with coarse mesh sizes (5 mm, 7.5 mm, and 10 mm). However, for the other three specimens, the maximum strain ε_f shows the same tendency, and they are in almost complete agreement. For these specimens, the maximum strain is found to be ε_f = 0.16, 0.12, and 0.11 when mesh sizes 5 mm, 7.5 mm, and 10 mm are used, respectively.

5.2 Failure definition

Figure 26 shows the engineering stress-strain for the Germanischer Lloyd (GL), Peschmann, Rice-Tracey and Cockcroft-Latham (RTCL), and ultimate strain criteria. Specimen 4 and AISI 1080 steel are used in this model. As observed in the figure, the RTCL criterion has the highest rupture strain, followed by the Peschmann and Germanischer Lloyd (GL) criteria. The initial crack in the specimens is indicated by a dashed line with a filled circle.

Figure 26c shows the engineering stress-strain curve obtained with the Rice-Tracey and Cockcroft-Latham (RTCL) criterion. The results indicate that the rupture strain with mesh size l_e = 2.5 mm shows a failure strain of ε_f = 0.39.

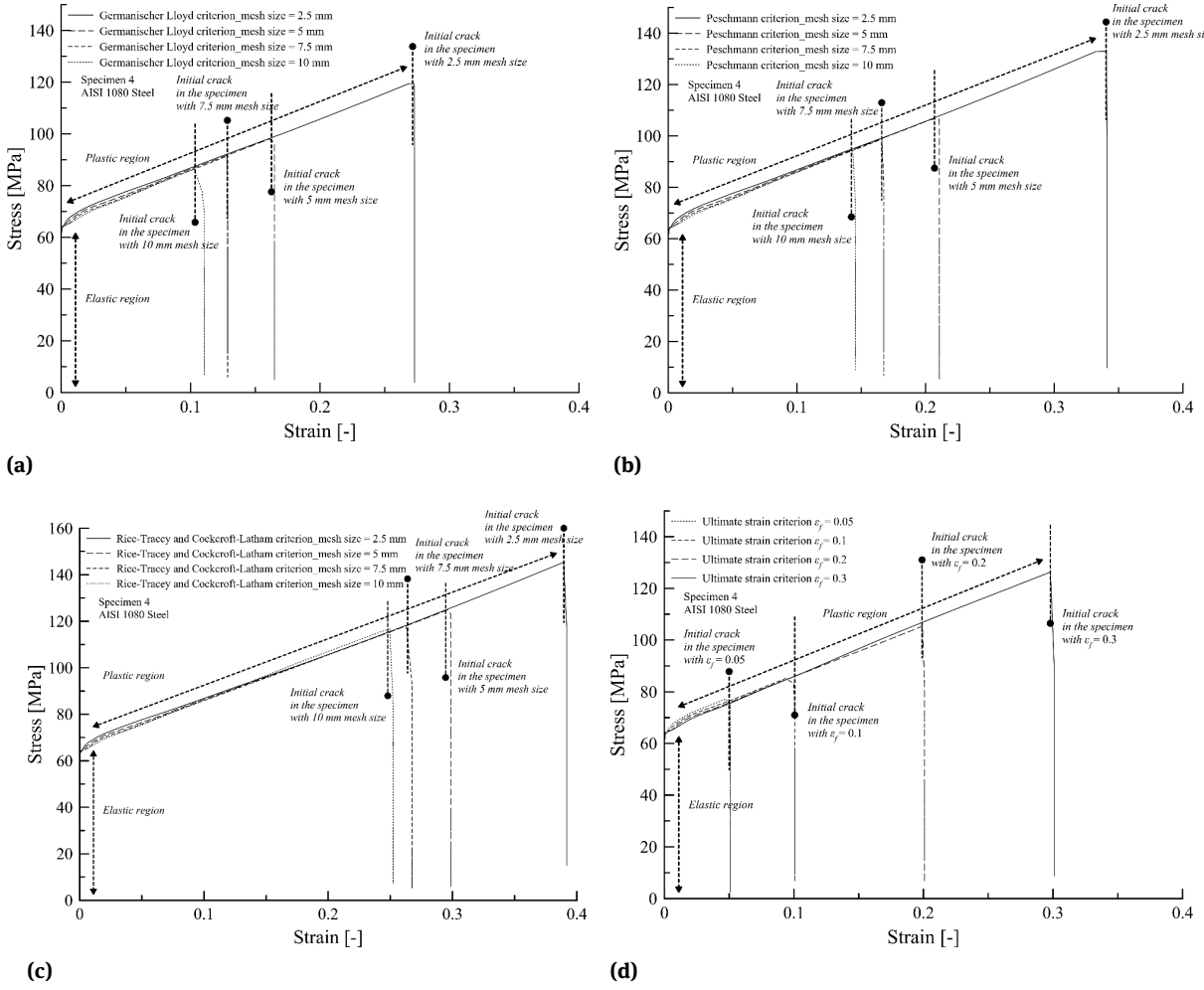

Figure 26: The stress-strain curves with the applied failure criterion and AISI 1080 steel on specimen 4. (a) Germanischer Lloyd (GL) criterion; (b) Peschmann criterion; (c) RTCL criterion; (d) ultimate strain criterion

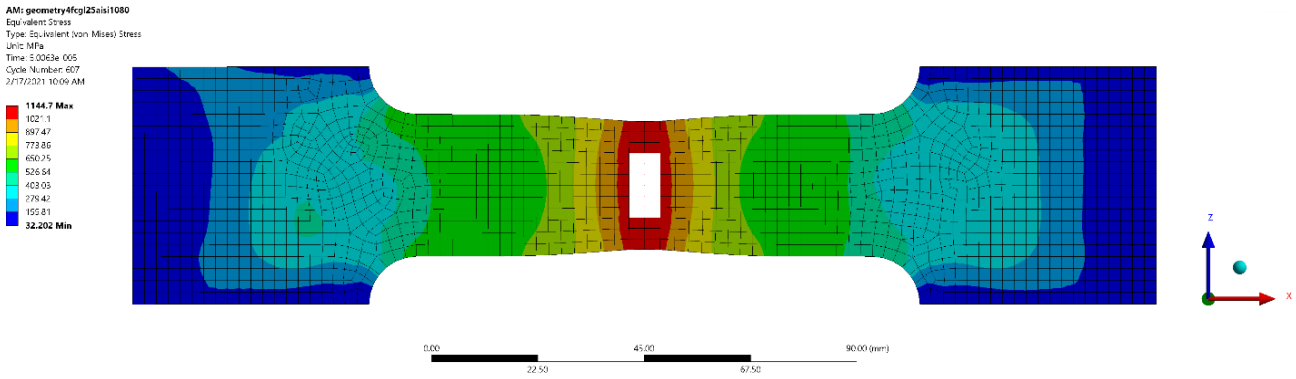

(a)

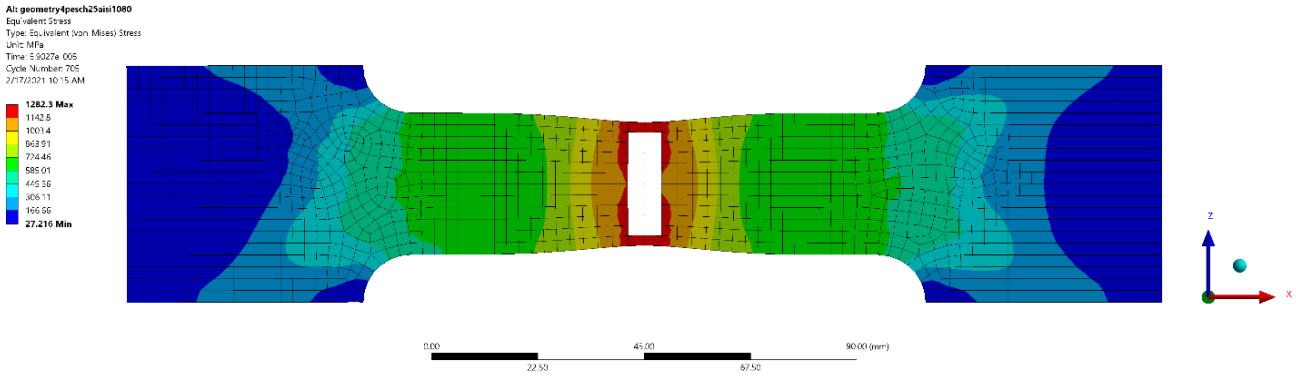

(b)

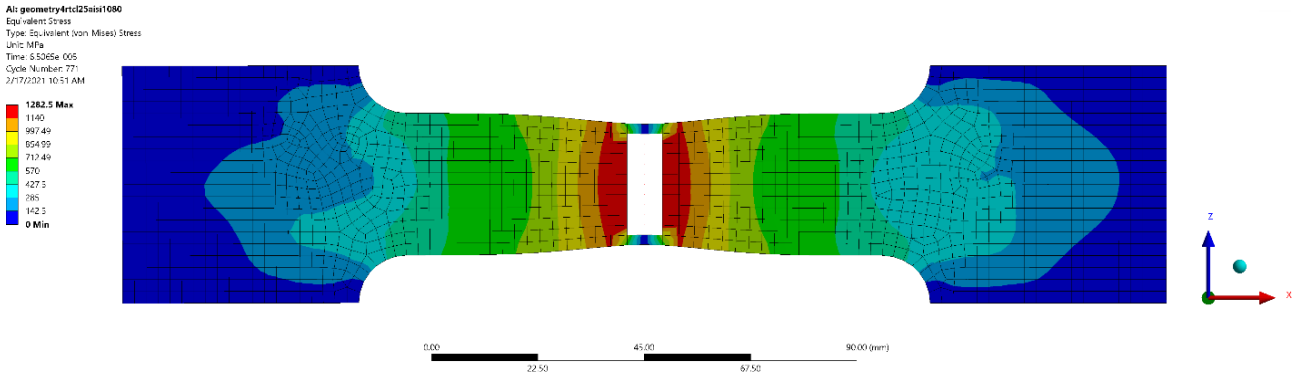

(c)

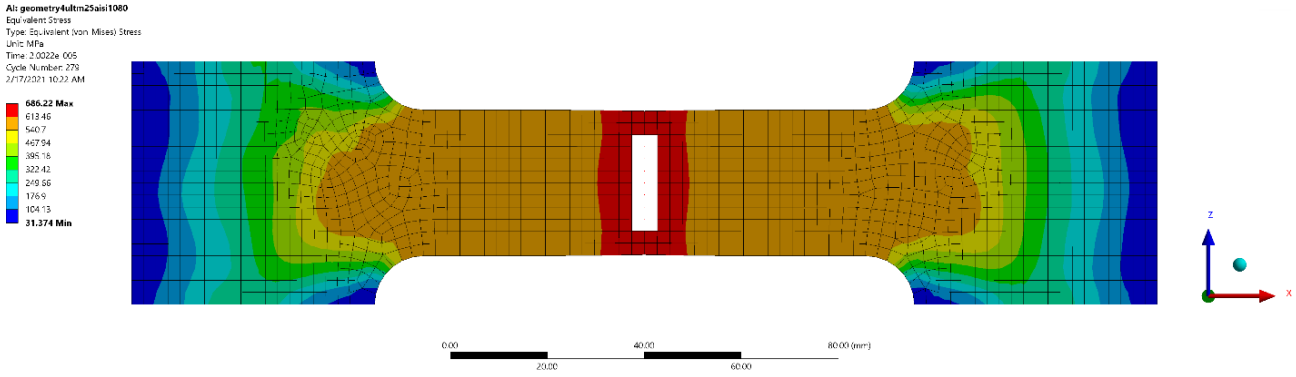

(d)

Figure 27: The von Mises stress distribution in the tensile test after a fracture occurs with 2.5 mm mesh size. (a) Germanischer Lloyd (GL) criterion; (b) Peschmann criterion; (c) RTCL criterion; (d) ultimate strain criterion

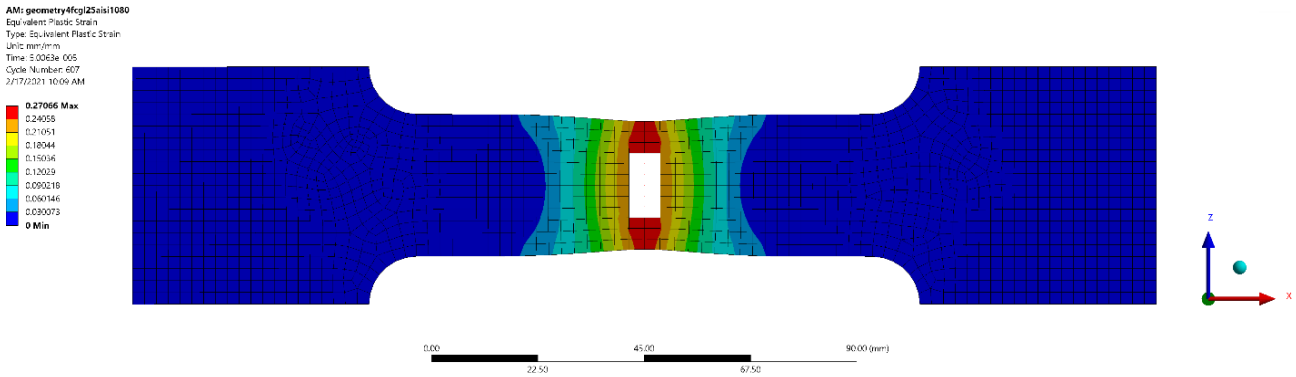

(a)

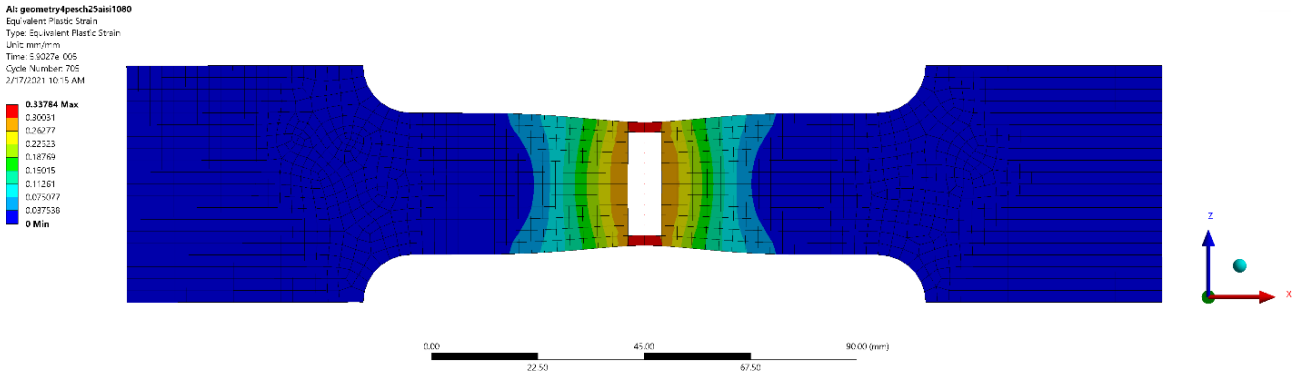

(b)

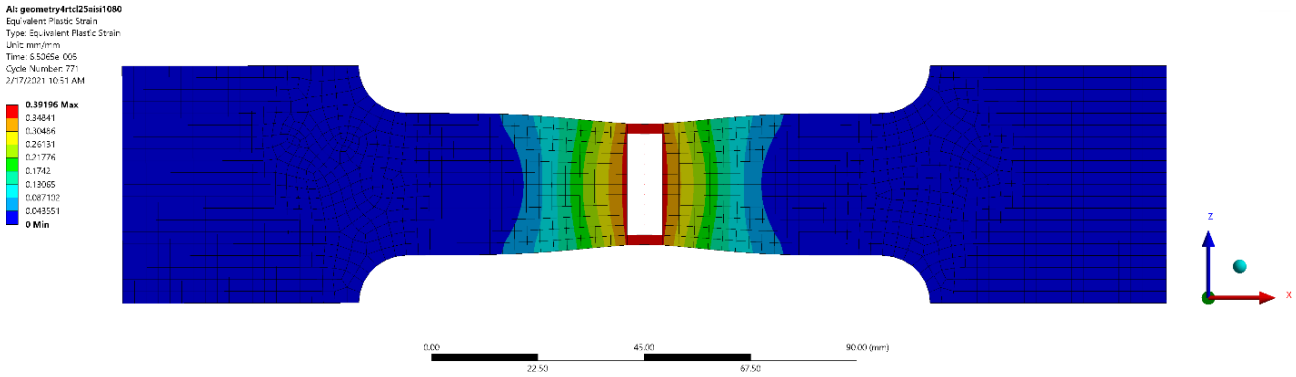

(c)

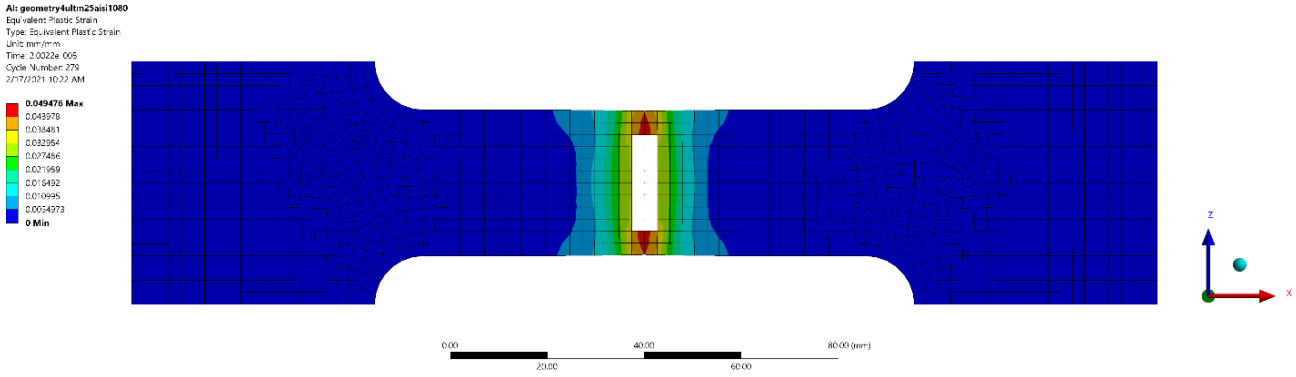

(d)

Figure 28: The maximum strain distribution in the tensile test after a fracture occurs with 2.5 mm mesh size. (a) Germanischer Lloyd (GL) criterion; (b) Peschmann criterion; (c) RTCL criterion; (d) ultimate strain criterion

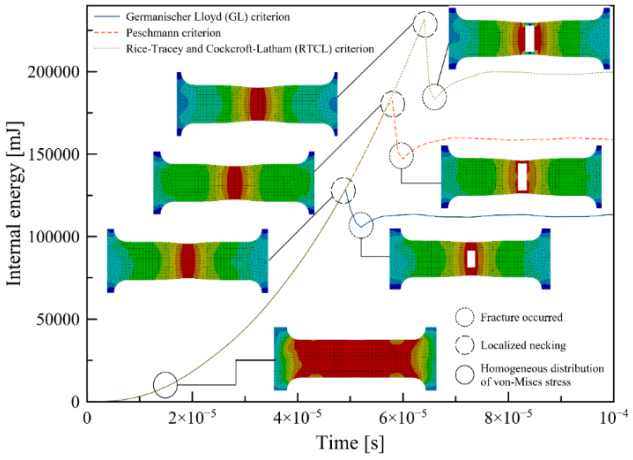

Figure 29: The internal energy generated during simulation with 2.5 mm mesh size

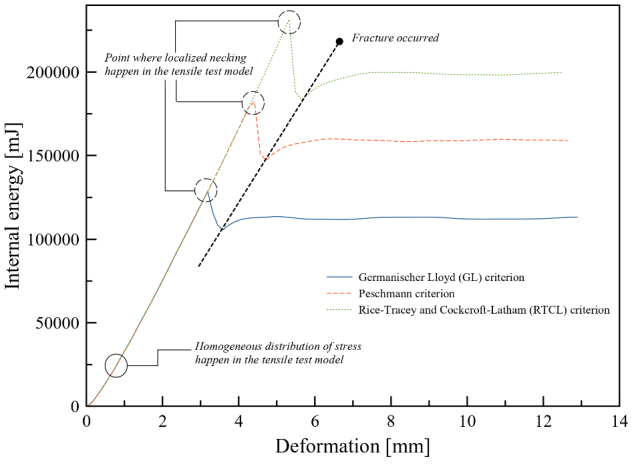

Figure 32: The internal energy versus deformation curve

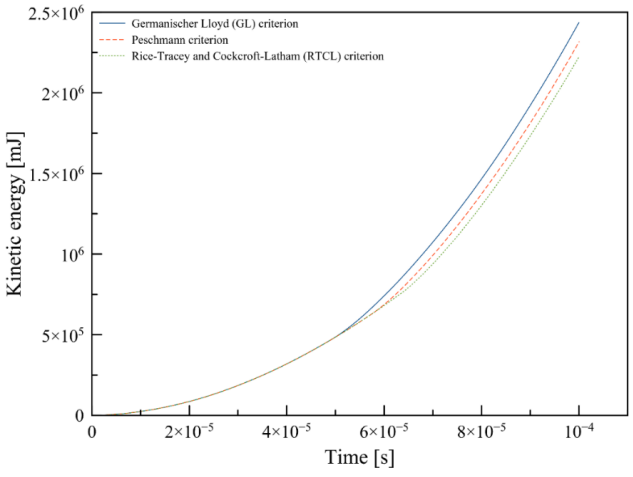

Figure 30: The kinetic energy generated during simulation

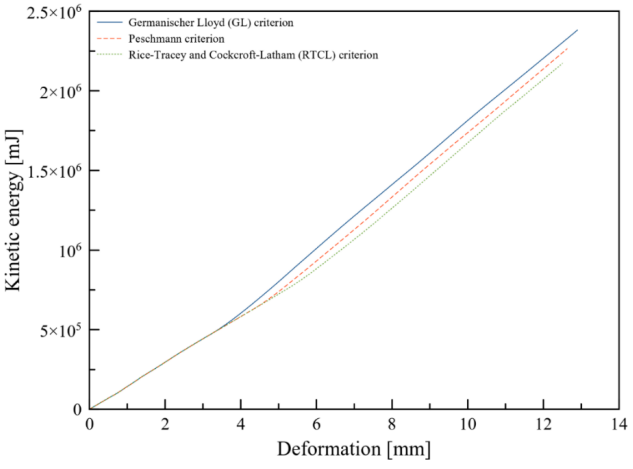

Figure 33: The kinetic energy versus deformation curve

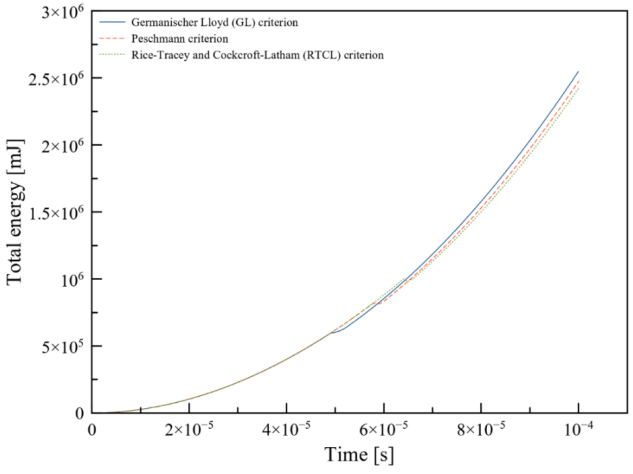

Figure 31: The total energy generated during simulation

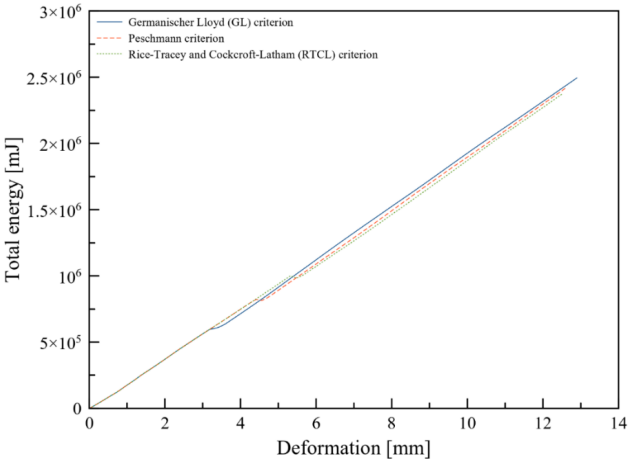

Figure 34: The curve of total energy versus deformation

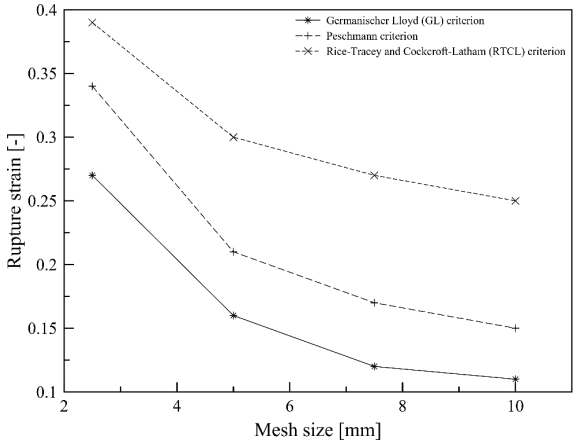

Figure 36: Rupture strain based on mesh size thickness for the three well-known failure criteria in damaged ship structure

However, the Peschmann and Germanischer Lloyd (GL) criteria show smaller rupture strain values. The Peschmann and Germanischer Lloyd (GL) criteria result in $\varepsilon_f = 0.34$ and 0.27 when a mesh size of 2.5 mm is used, as shown in Figure 26b and 26a, respectively. On the other hand, extremely small failure strains, such as 0.05, 0.1, 0.2, and 0.3, can be effectively handled by the ultimate strain criterion, as shown in Figure 26d.

Figures 27 and 28 show the von Mises stress and the strain contours obtained with the four failure criteria after the fracture occurs. The snapshot shows a mesh size of 2.5 mm. As is shown in Figure 27, the gauge length of specimen 4 experiences the highest von Mises stress. Furthermore, the results suggest that the Germanischer Lloyd (GL) criterion results in small crack propagation in the specimen, as presented in Figure 27a. This condition is slightly different

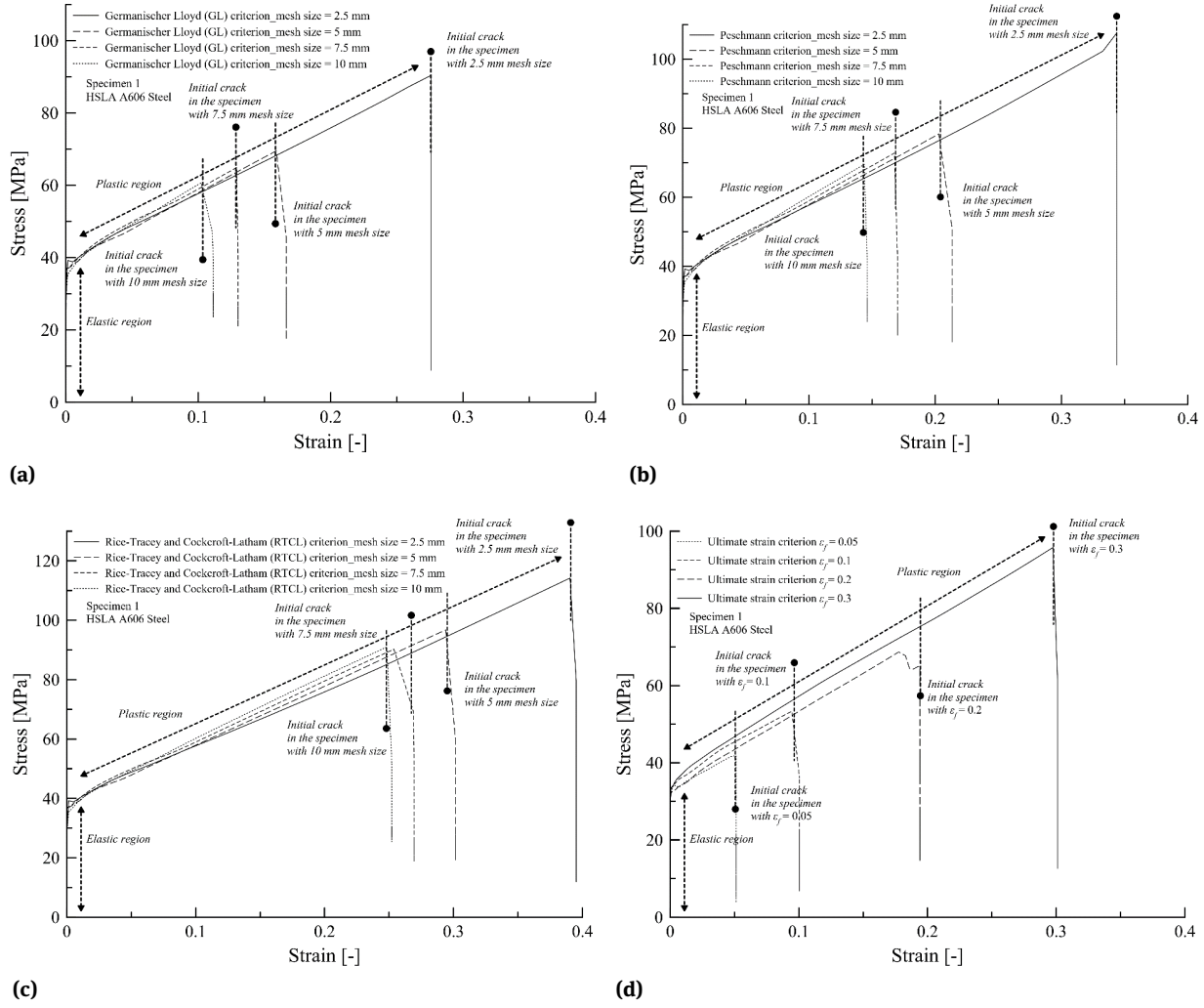

Figure 35: The stress-strain curve with different mesh sizes and HSLA A606 steel on specimen 1. (a) Germanischer Lloyd (GL) criterion; (b) Peschmann criterion; (c) RTCL criterion; (d) ultimate strain criterion

from the Peschmann and Rice-Tracey and Cockcroft-Latham (RTCL) criteria, which are shown in Figure 27b and 27c. The Rice-Tracey and Cockcroft-Latham (RTCL) criterion results in slightly larger crack propagation, followed by the Peschmann and Germanischer Lloyd (GL) criteria. On the other hand, with the ultimate strain $\varepsilon_f = 0.05$, as shown in Figure 27d, localized necking is not quite visible in the fracture region. However, von Mises stress is clearly observed to be homogenously distributed throughout the gauge length.

Figure 29 shows the internal energy generated during the simulation. This internal energy increases to a certain point when the specimen is under tension. The results indicate that the Germanischer Lloyd (GL) criterion generates the lowest internal energy. Localized necking appears to start at the internal energy of 128 joules, followed by a decrease in energy, and then the fracture occurs at 105 joules. This phenomenon shows much lower internal energy compared with the Peschmann and Rice-Tracey and Cockcroft-Latham (RTCL) criteria. It is also seen in Figure 29 that the highest internal energy is obtained with the Rice-Tracey and Cockcroft-Latham (RTCL) criterion, followed by the Peschmann criterion. With Rice-Tracey and Cockcroft-Latham (RTCL), localized necking starts at the internal energy of 231 joules. Afterward, the energy decreases to 183 joules, and the initial fracture occurs. On the other hand, with the Peschmann criterion, localized necking starts at the internal energy of 182 joules, and the initial fracture occurs at 147 joules.

Figure 30 shows the kinetic energy obtained in the simulation. As observed in the figure, the three criteria have identical energy values of 523 joules until 5.2×10^{-5} seconds. Afterward, the Germanischer Lloyd (GL) criterion produces slightly higher energy, followed by Peschmann and Rice-Tracey and Cockcroft-Latham (RTCL) criteria, indicated by the blue, red, and green lines, respectively. The total energy is observed to have the same trend, as presented in Figure 31. The criteria have identical total energy values of 596 joules until 4.9×10^{-5} s at the end of the simulation. Then, the results suggest that the Germanischer Lloyd (GL) criterion produces slightly higher total energy, followed by Peschmann and Rice-Tracey and Cockcroft-Latham (RTCL) criteria. Figures 32, 33, and 34 show the curves of internal energy, kinetic energy, and total energy versus deformation, respectively.

5.3 Meshing size

It is essential to study the mesh sensitivity of crack growth behavior of a ductile fracture in a material. Different levels of mesh refinement influence solution convergence [56]. Particular attention is dedicated to mesh effects on the crack initiation and rupture strain in the damaged ship structure under different known failure criteria.

Figure 35 presents the engineering stress-strain for the four failure criteria with different mesh sizes for specimen 1 and HSLA A606 steel. The results indicate that the Germanischer Lloyd (GL), Peschmann, and Rice-Tracey and Cockcroft-Latham (RTCL) criteria obtain a small rupture strain value along with an increase in the meshing size, as shown in Figure 35a, 35b, and 35c, respectively.

Figure 36 shows the rupture strain with different mesh sizes for the three failure criteria. Rupture strain occurs at 0.27, 0.34, and 0.39 for the Germanischer Lloyd (GL), Peschmann, and RTCL criteria, respectively, with 2.5 mm mesh size. The simulation using the coarser mesh of 10 mm appears to produce rupture strains at 0.11, 0.15, and 0.25, respectively. As shown in the figure, the Peschmann criterion has considerably higher rupture strain ε_f at a smaller mesh size l_e than the rupture strain ε_f obtained for the Germanischer Lloyd (GL). In Figure 36, these two failure criteria are indicated with a dashed line and a solid line, respectively.

5.4 Overall discussion

The findings of this study suggest that the FEA results are influenced by the geometry of the investigated specimen. Specimen 2, which has the shortest gauge length, shows an earlier rupture strain. When compared with other specimens, this rupture strain value tends to be quite small. However, this shortcoming in specimen 2 can be overcome by the 2.5 mm mesh size, which appears to result in the same value for the rupture strain, 0.27. As was proved in [10], the mesh size significantly affects the results of the finite element method. Furthermore, it is likely that this dissimilarity occurs because the coarse meshes, 5 mm, 7.5 mm, and 10 mm, do not completely cover the gauge length of specimen 2, as illustrated in Figure 25b. These mesh sizes are also slightly larger than the gauge length of 4 mm. This condition can also be recognized by the presence of strain in the grip section near the gauge length of specimen 2, as shown in Figure 25b.

The finding of the study on the failure criteria shows that the RTCL criterion produces a slightly higher rupture strain, followed by the Peschmann and Germanischer Lloyd (GL) criteria, as shown in Figure 26b and 26a. The results also suggest that the criterion based on the maximum stress produces a slightly larger rupture strain compared with the criteria based on maximum strain. RTCL is observed to have a rupture strain of $\varepsilon_f = 0.39$ for $l_e = 2.5$ mm. The Peschmann and Germanischer Lloyd (GL) criteria have slightly smaller

rupture strain values of 0.34 and 0.27, respectively. Furthermore, this difference in the rupture strain value appears to affect crack propagation, and in turn, crack propagation likely affects the internal energy during the tensile test. As shown in Figures 27 and 29, Germanischer Lloyd (GL) has smaller crack propagation and lower internal energy when compared with the Peschmann and Rice-Tracey and Cockcroft-Latham (RTCL) criteria. This effect of rupture strain on crack propagation is in accordance with the literature [18]. More evidence shows that localized necking is initiated at the internal energy of 128 joules for the GL. This value is the lowest obtained. Higher internal energy of 147 joules and 231 joules is observed for the Peschmann and RTCL, respectively, when localized necking occurs. In the ultimate strain criterion, the proposed rupture strain is extremely small, ranging from 0.05 to 0.35. Therefore, this criterion is distinctive from the others. The results suggest that this failure criterion can still be used even though the rupture strain is quite small (0.05). No constraints were found on these values. Surprisingly, with this failure value, the stress distribution is observed throughout almost the entire specimen. In this study, the effect of specimen thickness was not the main focus and was not investigated. However, the results indicate that the thickness of the specimen affects the failure strain, as discussed in Section 2.6.

Figures 37–40 show the states of the material as it approaches failure during the simulation with the described failure criteria. It can be seen that the strain is concentrated in the center of the gauge length, and at the maximum elongation, the first deleted elements are different. This phenomenon likely occurs due to differences in the value of the failure strain.

The finding of the study on the failure criteria with different mesh sizes suggests that the GL, Peschmann, and RTCL criteria depend on the selected mesh size. The coarser mesh appears to produce an earlier rupture strain compared with the finer mesh. For the Germanischer Lloyd (GL) criterion, the results indicate that the rupture strain has a value of 0.27 when 2.5 mm mesh size is used, whereas it is 0.11 with the coarser mesh of 10 mm. The rupture strain is also slightly higher when 2.5 mm mesh size is used with the Peschmann and RTCL criteria, obtaining values of 0.34 and 0.39, respectively, compared with the 10 mm mesh (0.15 and 0.25).

In the extended study, several classical papers are relevant to the analysis of failure progress. Tvergaard and Needleman [57] investigated the ductile fracture process in

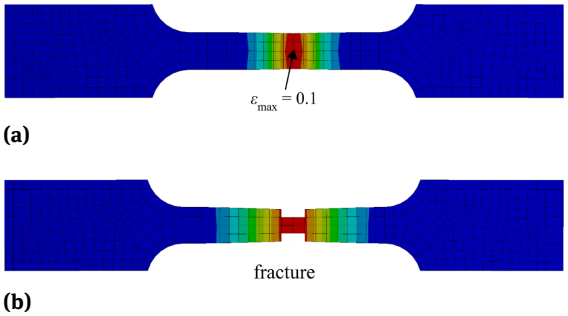

Figure 37: The steps of failure during the simulation with the Germanischer Lloyd (GL) criterion and 2.5 mm mesh size: (a) maximum strain = 0.1; (b) fracture occurs

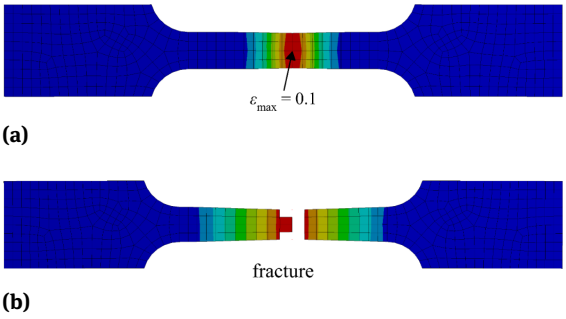

Figure 38: The steps of failure during the simulation with the Peschmann criterion and 2.5 mm mesh size: (a) maximum strain = 0.1; (b) fracture occurs

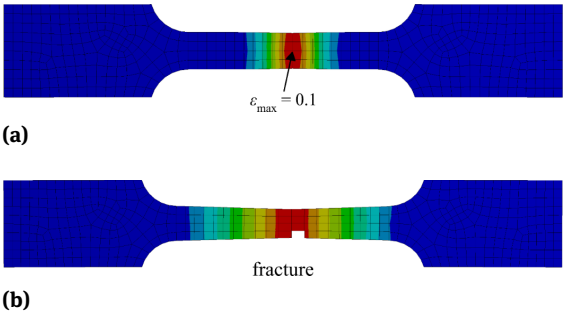

Figure 39: The steps of failure during the simulation with the Rice-Tracey and Cockcroft-Latham (RTCL) criterion and 2.5 mm mesh size: (a) maximum strain = 0.1; (b) fracture occurs

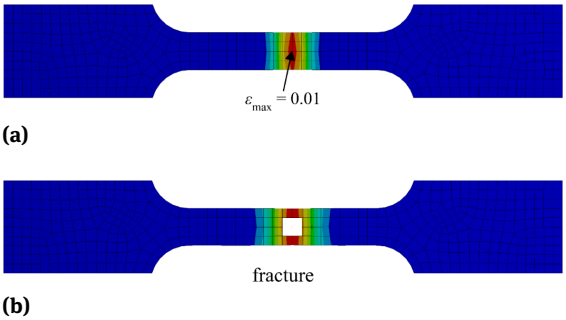

Figure 40: The steps of failure during the simulation with the ultimate failure criterion $\varepsilon = 0.05$ and 2.5 mm mesh size: (a) maximum strain = 0.01 and (b) fracture occurrence

a round tensile test specimen. The observation revealed that if the bar had a uniform thickness with no porosity, then necking occurred. Later, a penny-shaped crack formed, and the zig-zag growth of the crack gave rise to a conical void-sheet fracture. The relation between crack growth resistance and fracture process parameters specifying the traction- the separation law of the fracture process in elastic-plastic solids- was further evaluated by Tvergaard and Hutchinson [58]. In the study of crack growth, Rice [59] introduced the J-integral as a parameter for describing crack propagation in elastic-plastic fracture mechanics conditions. The J-integral was first proposed as a fracture criterion for small-scale plasticity conditions at the crack tip. Subsequently, it was applied as a fracture criterion to study fracture initiation and stable crack growth in large-scale plasticity. Moreover, approximate constitutive equations of localization, as important mechanisms of ductile fracture, have been evaluated in plane strain tests using several methods, including the Gurson model [60], flow localization using J_2 corner theory, and Storen and Rice [61].

6 Conclusions

The selection of the geometry of the specimen for the tensile test is an important factor to consider. A larger mesh size compared with the specimen geometry can provide unsatisfactory results relative to smaller mesh size, as occurred in specimen 2. Furthermore, this study also shows that failure criteria based on the maximum stress produce a slightly higher rupture strain compared with those based on the maximum strain. The highest rupture strain value was obtained with Rice-Tracey and Cockcroft-Latham (RTCL), followed by Peschmann and Germanischer Lloyd (GL). These changes in the rupture strain value also appear to affect the crack propagation and the internal energy generated. Furthermore, the selection of the mesh size was also studied because it strongly influences these failure criteria. The use of a coarser mesh size resulted in a smaller rupture strain. Further research is needed to determine the influence of the thickness of the tensile test specimen, which was not explored in this study.

Acknowledgement: This work was supported by the RKAT PTNBH Universitas Sebelas Maret - Year 2022, under Research Scheme of "Penelitian Kolaborasi Internasional" (KI-UNS), with Research Grant/Contract No. 254/UN27.22/PT.01.03/2022. The support is gratefully acknowledged by the authors.

Author contributions: All authors have read and agreed to the published version of the manuscript.

Conflict of interest: The authors state no conflict of interest.

References

[1] UNCTAD. Review of Maritime Transport 2019. Geneva: United Nations Publication; 2019.
[2] Calle MA, Verleysen P, Alves M. Benchmark study of failure criteria for ship collision modeling using purpose-designed tensile specimen geometries. Mar Structures. 2017;53:68–85.
[3] Hooper JJ, Foecke T, Graham L, Weihs TP. The metallurgical analysis of wrought iron from the RMS Titanic. Meas Sci Technol. 2003;14(9):1556–63.
[4] IMO. *International Convention for the Safety of Life at Sea (SOLAS)*. London: IMO Publications; 2010.
[5] Yip TL, Talley WK, Jin D. The effectiveness of double hulls in reducing vessel-accident oil spillage. Mar Pollut Bull. 2011 Nov;62(11):2427–32.
[6] Zhang S, Pedersen PT, Villavicencio R. Probability and Mechanics of Ship Collision and Grounding. UK: Elsevier; 2019.
[7] Minorsky VU. An Analysis of Ship Collisions with Reference to Nuclear Power Plants. J Ship Res. 1959;3(2):1–4.
[8] Lehmann E, Peschmann J. Energy absorption by the steel structure of ships in the event of collisions. Mar Struct. 2002;15(4–5):429–41.
[9] Ehlers S. The influence of the material relation on the accuracy of collision simulations. Mar Struct. 2010;23(4):462–74.
[10] Storheim M, Amdahl J, Martens I. On the accuracy of fracture estimation in collision analysis of ship and offshore structures. Mar Struct. 2015;44:254–87.
[11] Prabowo AR, Bae DM, Sohn JM, Zakki AF, Cao B, Cho JH. Effects of the rebounding of a striking ship on structural crashworthiness during ship-ship collision. Thin-walled Struct. 2017;115:225–39.
[12] Prabowo AR, Baek SJ, Byeon JH, Bae DM, Cho JH, Sohn JM. Investigation on the Structural Damage of a Double-Hull Ship, Part i - Ship Collision. Procedia Struct Integr. 2017;5:935–42.
[13] Ringsberg JW, Amdahl J, Chen BQ, Cho SR, Ehlers S, Hu Z, et al. Zhang, S. MARSTRUCT benchmark study on nonlinear FE simulation of an experiment of an indenter impact with a ship side-shell structure. Mar Struct. 2018;59:142–57.
[14] Marinatos JN, Samuelides MS. Towards a unified methodology for the simulation of rupture in collision and grounding of ships. Mar Struct. 2015;42:1–32.
[15] Calle MA, Alves M. A review-analysis on material failure modeling in ship collision. Ocean Eng. 2015;106:20–38.
[16] Vredeveldt A, Feenstra E. Crashworthy side structures for improved collision damage survivability of coasters and medium sized Ro-Ro cargo ship. Report GRD1-1999-10566, TNO/UNI, Netherlands; 2001.
[17] Peschmann J, Kulzep A. Final report for BMBF Life-Cycle Design. Part D2A: Side Collision of Double Skin Ships. Technical University of Hamburg; 2000.
[18] Ehlers S, Broekhuijsen J, Alsos HS, Biehl F, Tabri K. Simulating the collision response of ship side structures: A failure criteria

benchmark study. Int Shipbuild Prog. 2008;55(1–2):127–44.
[19] Prabowo AR, Sohn JM, Bae DM, Setiyawan A. Crashworthiness assessment of thin-walled bottom structures during powered-hard grounding accidents. Proceedings of the International Conference on Offshore Mechanics and Arctic Engineering (OMAE); 2018 Jun 17-22; Madrid, Spain. ASME, 2018. https://doi.org/10.1115/OMAE2018-77492.
[20] Törnqvist R. Design of crashworthy ship structures [dissertation]. Lyngby, Denmark: Technical University of Denmark; 2003.
[21] Rice JR, Tracey DM. On the ductile enlargement of voids in triaxial stress fields. J Mech Phys Solids. 1969;17(3):201–17.
[22] Cockcroft MG, Latham DJ. Ductility and the workability of metals. J Inst Met. 1968;96(1):33–9.
[23] Wen HM, Jones N. Experimental investigation of the scaling laws for metal plates struck by large masses. Int J Impact Eng. 1993;13(3):485–505.
[24] Amdahl J, Kavlie D. Experimental and numerical simulation of double hull stranding. DNV MIT Workshop on Mechanics of Ship Collision and Grounding; 1992-Sep 16-17; Oslo, Norway. DNV; 1992.
[25] Amdahl J. Side collision. 22nd WEGEmT Graduate School, Technical University of Denmark; 1995.
[26] Zhang S. The Mechanics of Ship Collisions [dissertation]. Lyngby, Denmark: Technical University of Denmark; 1999.
[27] Ridwan R, Prabowo AR, Muhayat N, Putranto T, Sohn JM. Tensile analysis and assessment of carbon and alloy steels using fe approach as an idealization of material fractures under collision and grounding. Curved Layer Struct. 2020;7(1):188–98.
[28] Prabowo AR, Bae DM, Sohn JM, Zakki AF, Cao B, Wang Q. Analysis of structural behavior during collision event accounting for bow and side structure interaction. Theor Appl Mech Lett. 2017;7(1):6–12.
[29] Prabowo AR, Sohn JM, Bae DM, Cho JH. Estimating structure response and progressive failure of a ship hull under side-bow collisions. Teh Vjesn. 2018;25(5):1513–22.
[30] Zienkiewicz OC, Taylor RL, Zhu JZ. The Finite Element Method: Its Basis and Fundamentals. 6^{th} ed. Oxford: Elsevier; 2005.
[31] Crisfield MA. Non-linear Finite Element Analysis of Solids and Structures. Chichester: John Wiley & Sons; 1991.
[32] Simo JC. Numerical Analysis and Simulation of Plasticity. Amsterdam: Elsevier Science Publishers; 1995.
[33] Celentano D. A large strain thermoviscoplastic formulation for the solidification of S.G. cast iron in a green sand mould. Int J Plast. 2001;17(12):1623–58.
[34] ANSYS. ANSYS Explicit Dynamics Analysis Guide. Pennsylvania, USA: ANSYS Inc.; 2020.
[35] Callister WD, Rethwisch DG. *Materials science and engineering: an introduction*. 10^{th} ed. New York: John Wiley & Sons; 2018.
[36] Marciniak Z, Duncan JL, Hu SJ. Mechanics of sheet metal forming. Oxford: Elsevier ButtenNorth-Heinemann; 2002.
[37] Beddoes J, Bibby MJ. Principles of metal manufacturing processes. Oxford: Elsevier ButtenNorth-Heinemann; 1999.
[38] Tekkaya EA, Altan T. Sheet Metal Forming: Fundamentals. Volume I. Materials Park (OH): ASM International; 2012.
[39] Chang KH. e-Design: computer-aided engineering design. Oxford: Academic Press; 2015.
[40] AbuBakar A, Dow RS. The impact analysis characteristics of a ship's bow during collisions. Eng Fail Anal. 2019;100:492–511.
[41] Calle MA, Oshiro RE, Alves M. Ship collision and grounding: scaled experiments and numerical analysis. Int J Impact Eng. 2017;103:195–210.
[42] Ridwan, Putranto T, Laksono FB, Prabowo AR. Fracture and Damage to the Material accounting for Transportation Crash and Accident. Procedia Struct Integr. 2020;27:38–45.
[43] Vukelic G, Vizentin G, Murawski L, Recho N. Marine Structural Failures Database. Rijeka, Croatia: University of Rijeka; 2018.
[44] Alsos HS, Amdahl J. On the resistance to penetration of stiffened plates, Part I – Experiments. Int J Impact Eng. 2009;36(6):799–807.
[45] Wang Z, Hu Z, Liu K, Chen G. Application of a material model based on the Johnson-Cook and Gurson-Tvergaard-Needleman model in ship collision and grounding simulations. Ocean Eng. 2020;205:106768.
[46] Liu B, Guedes Soares C. Effect of strain rate on dynamic responses of laterally impacted steel plates. Int J Mech Sci. 2019;160:307–17.
[47] Bureau Veritas. NR216 Rules on Materials and Welding for the Classification of Marine Units. 2011.
[48] McDermott JF, Kline RG, Jones EL, Maniar NM, Chiang WP. Tanker Structural Analysis for Minor Collisions. New York: SNAME Transactions; 1974.
[49] Cabezas EE, Celentano DJ. Experimental and numerical analysis of the tensile test using sheet specimens. Finite Elem Anal Des. 2004;40(5–6):555–75.
[50] Wiegard B, Ehlers S. Pragmatic regularization of element-dependent effects in finite element simulations of ductile tensile failure initiation using fine meshes. Mar Struct. 2020;74:102823.
[51] Zhang M, Sun Q, Liu J, Hu Z, Zhang S. A study of the rupture behavior of a ship side plate laterally punched by a full-shape bulbous bow indenter. Ocean Eng. 2019;182:48–60.
[52] Iannucci L, Del Rosso S, Curtis PT, Pope DJ, Duke PW. Understanding the thickness effect on the tensile strength property of Dyneema®HB26 laminates. Materials (Basel). 2018 Aug;11(8):1431.
[53] Odefey M. Simulation of Collisions between RORO Vessels with Improved Double-Hull Designs [dissertation]. Gothenburg: Chalmers University of Technology; 2011.
[54] Ehlers S, Varsta P. Strain and stress relation for non-linear finite element simulations. Thin-walled Struct. 2019;47(11):1203–17.
[55] Ehlers S. Strain and stress relation until fracture for finite element simulations of a thin circular plate. Thin-walled Struct. 2010;48(1):1–8.
[56] Needleman A, Tvergaard V. Mesh effects in the analysis of dynamic ductile crack growth. Eng Fract Mech. 1994;47(1):75–91.
[57] Tvergaard V, Needleman A. Analysis of the cup-cone fracture in a round tensile bar. Acta Metall. 1984;2(1):157–69.
[58] Tvergaard V, Hutchinson JW. The relation between crack growth resistance and fracture process parameters in elastic-plastic solids. J Mech Phys Solids. 1992;40(6):1377–97.
[59] Rice JR. A Path Independent Integral and the Approximate Analysis of Strain Concentration by Notches and Cracks. J Appl Mech. 1968;35(2):379–86.
[60] Tvergaard V. On localization in ductile materials containing spherical voids. Int J Fract. 1982;18(4):237–52.
[61] Tvergaard V, Needleman A, Lo KK. Flow localization in the plane strain tensile test. J Mech Phys Solids. 1981;29(2):115–42.